Investigations towards a Single-CCD Pointing-Solution for the Medium-Sized Telescopes of the Cherenkov Telescope Array

Masterarbeit aus der Physik

Vorgelegt von
Domenico Tiziani
30.10.2015

Friedrich-Alexander-Universität Erlangen-Nürnberg

Betreuer: Prof. Dr. Christopher van Eldik
Zweitgutachterin: Prof. Dr. Gisela Anton

Abstract

The Cherenkov Telescope Array (CTA) is the next generation ground-based gamma-ray observatory that is currently in a pre-construction phase. It aims to measure cosmic gamma radiation in the energy regime between several tens of GeV to more than 100 TeV. It will consist of Cherenkov telescopes of three different sizes.

An important calibration for CTA is the pointing, which describes the exact alignment of a Cherenkov telescope and also the ability to transform a position in the sky to a point in the plane of the telescope camera and vice versa. One approach for the measurement of the pointing is the attachment of an optical CCD-camera to the telescope that captures the position of the Cherenkov camera and of the stars in the night sky simultaneously.

In this thesis, the adaptation of this method for the medium-sized telescopes of CTA is investigated. Therefore, the development of a housing for a pointing camera is described. A software library is introduced, that can be used for simulating images which can be captured by a CCD-camera. Furthermore, a wrapper-library for an open source software for astronomical image calibration is developed. With this library, the pointing can be reconstructed from the images of the stars. The quality of this reconstruction is tested both with simulated and with real images.

First result from simulated images show that the pointing can be determined with a median deviation of $0.6''$.

Zusammenfassung

Das Cherenkov Telescope Array (CTA) ist das bodengebundene Experiment der nächsten Generation zur Messung kosmischer Gammastrahlung im Energiebereich von einigen zehn GeV bis zu über 100 TeV. Es wird aus Teleskopen dreier verschiedener Größen bestehen. Das Projekt befindet sich gerade in der Entwicklungs- und Prototypenphase.

Eine wichtige Kalibrierung für CTA ist das sogenannte „Pointing“. Darunter versteht man sowohl die genaue Ausrichtung eines Cherenkov-Teleskops als auch die Fähigkeit, eine Position am Himmel in die Ebene der Cherenkov-Kamera zu transformieren und umgekehrt. Eine Methode, das Pointing zu messen, besteht darin, eine optische CCD-Kamera an das Teleskop zu montieren, die gleichzeitig die Position der Cherenkov-Kamera und der Sterne am Nachthimmel in einem Bild aufnimmt.

In dieser Arbeit wird die Adaptierung dieser Methode für die mittelgroßen CTA-Teleskope untersucht. Dafür wird die Entwicklung eines Gehäuses für eine solche Pointing-Kamera beschrieben. Es wird eine Software Bibliothek vorgestellt, mit deren Hilfe von einer Pointing-Kamera aufgenommene Bilder simuliert werden können. Zusätzlich wird eine Wrapper-Programmbibliothek für eine Open Source Software zur astronomischen Bildkalibrierung entwickelt, mit deren Hilfe das Pointing über die Sternpositionen rekonstruiert werden kann. Die Qualität dieser Rekonstruktion wird sowohl mit simulierten als auch mit reellen Bildern überprüft.

Erste Ergebnisse aus Simulationen zeigen, dass das Pointing mit dieser Methode bis auf eine mediane Abweichung von $0{,}6''$ bestimmt werden kann.

Contents

1 Introduction 5

2 VHE Gamma-Ray Astronomy 6
- 2.1 Sources of High Energetic Cosmic Gamma Rays 6
- 2.2 Production Mechanisms of VHE Gamma Rays 9

3 Imaging Atmospheric Cherenkov Telescopes 10
- 3.1 Electromagnetic Showers 10
- 3.2 Cherenkov Radiation 12
- 3.3 Detection Principle of IACTs 13
- 3.4 Pointing and Tracking 13
- 3.5 The Cherenkov Telescope Array 17

4 A Pointing Solution for the MST 20
- 4.1 Camera Hardware 20
  - 4.1.1 CCD-Camera 20
  - 4.1.2 Sensor 21
  - 4.1.3 Photographic Objective 21
- 4.2 Development of a Housing 22
  - 4.2.1 First Prototype 23
  - 4.2.2 Optimization of Thermal Conductivity 24
  - 4.2.3 Further Improvements to the Housing 26
- 4.3 Summary 26

5 Simulation and Analysis of Pointing Images 27
- 5.1 Parameters and Classes 27
- 5.2 Star Positions 28
- 5.3 Coordinate Transformations 28
- 5.4 Filling the Histogram of the Exposure 30
- 5.5 Output and Performance 32
- 5.6 Astrometry.net 32
- 5.7 Wrapper Library 33
- 5.8 Outlook 33
- 5.9 Summary 35

6 Towards a Verification and Validation of Pointing Reconstructions 36
- 6.1 Test of the Algorithm 36

6.2 Adding a Cherenkov Camera 38
6.3 Changing the Index Files 39
6.4 Simulating Different Magnitudes 40
6.5 Exposure and Aperture 41
6.6 Calibration Errors within a Pointing Image 43
6.7 Summary 45

7 Real Images of the Sky 46
7.1 Test Setup in Bamberg 46
7.2 Exemplary Comparison with the Simulation 46
7.3 Pointing Scan of the Sky 49
7.4 Summary 51

8 Summary and Outlook 52

Appendices 55

A Product Datasheet CCD-Camera 55

B Product Datasheet CCD-Sensor 59

C UML Class Diagram of Simulation 61

D Exposure and Aperture Results 63

E Global Rotation Errors in Calibrated Images 65

Bibliography 67

1 Introduction

Astronomers have been striving for an understanding of the world beyond our planet for thousands of years. While in the beginning being limited to just their eye-sight, they started to develop more and more sophisticated instruments and methods to observe celestial objects. By inventing the telescope in the 17th century, it became possible to see smaller and fainter structures. With better understanding of electromagnetism, astronomers wanted to expand observations of the sky to different wavelengths. Hence, they built the first radio telescopes which were able to detect radiation in the range of 1 mm (10^{-3} eV) up to about 100 m (10^{-8} eV). Apart from the radio regime, the visible spectrum, and some narrow bands in the infrared wavelengths, photons are strongly absorbed by the earth's atmosphere. Therefore, measurements of other energy regimes only became possible with aeronautics and Earth-orbiting satellites in the 1970's. Today, there is a variety of astronomical instruments orbiting the earth, expanding the detectable electromagnetic spectrum to infrared, ultraviolet, X-ray, and gamma radiation.

One big drawback of spaceborne gamma-ray telescopes is the technical limitation of their detector areas. Since the flux of very-high-energy (VHE) photons decreases with a power law and the flux of photons with energies > 100 GeV $= 10^9$ eV is too low, it is not possible to observe this energy regime using these instruments. Therefore, in the 1950's, another detection technique has been developed, namely the *Imaging Atmospheric Cherenkov Technique* (IACT). Cherenkov telescopes use the earth's atmosphere as an active detector medium, taking advantage of the fact that incoming gamma rays produce charged, secondary particles which propagate faster than the speed of light in the air and emit Cherenkov light. The latter can be collected with large mirrors focused on cameras that allow for very short exposure times in the order of nanoseconds.

The *Cherenkov Telescope Array* (CTA) is the next generation gamma-ray observatory that is currently in a pre-construction phase and will be built, starting in 2016. It will consist of two arrays of telescopes: one on the northern and one on the southern hemisphere. Each of the two arrays will consist of several tens of telescopes with mirror dishes of three different sizes.

One important calibration for CTA is the so-called *pointing.* This describes the ability to calculate the origin in the sky of an incoming gamma quantum from the Cherenkov light that has been mapped to the telescope cameras. This is accomplished with optical CCD cameras that track the exact orientation of the telescopes and their deformations. The main subject of this thesis is the characterization of a concept that uses only one CCD camera per telescope for the medium-sized telescopes of CTA. A housing for such a CCD camera which resists the environmental conditions of the instrument is developed. Furthermore, software libraries for simulating and analyzing images which can be captured with such a camera are developed and tested.

2 VHE Gamma-Ray Astronomy

Very-high energetic (VHE) gamma rays are photons in the energy range from about 100 GeV to 10 TeV. The following chapter gives a short overview of known sources of very-high energetic gamma radiation and describes how this radiation is produced.

2.1 Sources of High Energetic Cosmic Gamma Rays

While lower energy photons can in principle be emitted thermally, there is no known source being hot enough to radiate gamma quanta of more than $\sim 10^5$ eV by black-body radiation. (A black body with its peak energy of maximum flux at this energy would have a temperature of > 200000 K.) Consequently, these cosmic gamma rays can only be produced in transitions of atomic nuclei or interactions between elementary particles, making their sources not only interesting for astronomy, but also for particle physics.

Cosmic gamma rays are secondary products that are created by high energetic, charged particles produced in cosmic particle accelerators. These primary particles, misleadingly also known as *Cosmic Rays*, are generated in various astrophysical processes, some of which are described below. A map of the currently more than 160 known VHE sources can be seen in Figure 2.1.

Supernova Remnants

When a massive star reaches the end of its lifetime and the nuclear fusion reactions in its core cease, the core of the star collapses (Longair 1994). If the star is massive enough, i.e. it has more than about eight solar masses, the collapse does not stop at the state of a white dwarf, as it is the case for lighter stars. The density and temperature in the core become so great that the inverse β-decay becomes important. In this reaction, protons interact with energetic electrons and produce neutrons and neutrinos:

$$\mathrm{p} + \mathrm{e}^- \rightarrow \mathrm{n} + \nu_\mathrm{e} \tag{2.1}$$

Almost the entire matter of the core is transformed into neutrons and a neutron star is created.

The energy that originates from the collapse is deposited in the outer layers of the star. They are heated to a high temperature and expelled at velocities of about $(10-20)\cdot 10^3$ km/s. This violent process is called *supernova* (SN). The outer layers then expand spherically, sweep up mass from surrounding interstellar gas, and form a forward shock wave and a reverse shock wave which is caused by the deceleration of the

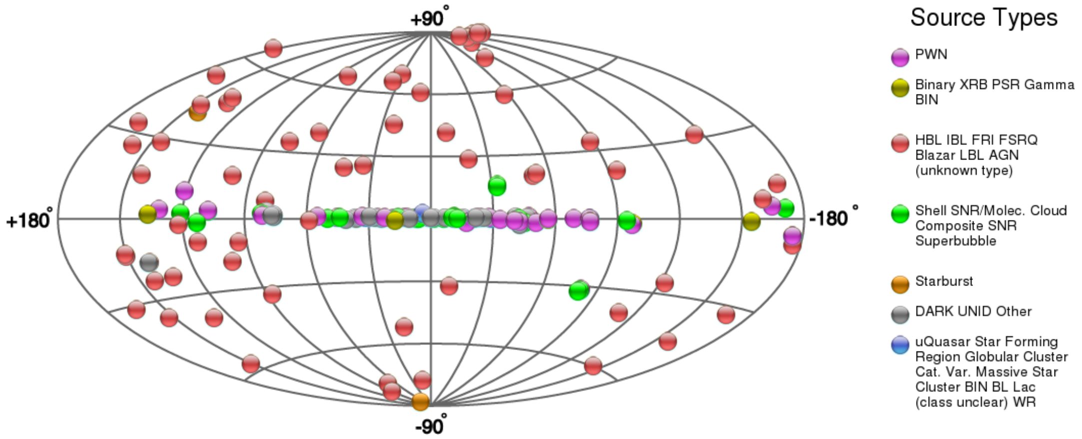

Figure 2.1: Sources in the TeV gamma-ray sky in galactic coordinates. (`http://tevcat.uchicago.edu`)

ejected materials and travels inwards (Castro et al. 2011). Once the swept-up mass becomes greater than the initially ejected mass, the supernova remnant (SNR) enters the Sedov-Taylor phase in which it expands adiabatically (Sedov 1959; Taylor 1950). In this phase, the SNR accelerates particles that are scattered back and forth between turbulent magnetic fields on both sides of the shock front.

Pulsar Wind Nebulae

When a neutron star is formed, its moment of inertia decreases with its strongly reduced radius in comparison to the original star. Thus, to conserve its angular momentum, the neutron star rotates very rapidly – up to hundreds of times per second. During the collapse, the magnetic field of the star is also compressed and can reach strengths up to 10^9 T (Longair 1994; Karttunen et al. 2001). If the magnetic field is tilted in respect to the rotational axis of the neutron star, a beam of electromagnetic radiation is emitted. Whenever this beam coincides with the line of sight, a short radio pulse can be detected on earth, giving this subclass of neutron stars the name *pulsar*.

The rapidly rotating magnetic field can also accelerate charged particles to relativistic energies. In interactions with surrounding matter, these relativistic particles can develop shock fronts in which further particles can be accelerated to even higher energies by the mechanism described above (Rees & Gunn 1974). Such an object is called a *pulsar wind nebula*.

The most prominent example for a pulsar wind nebula is the Crab Nebula that originated from a supernova which was observed in 1054.

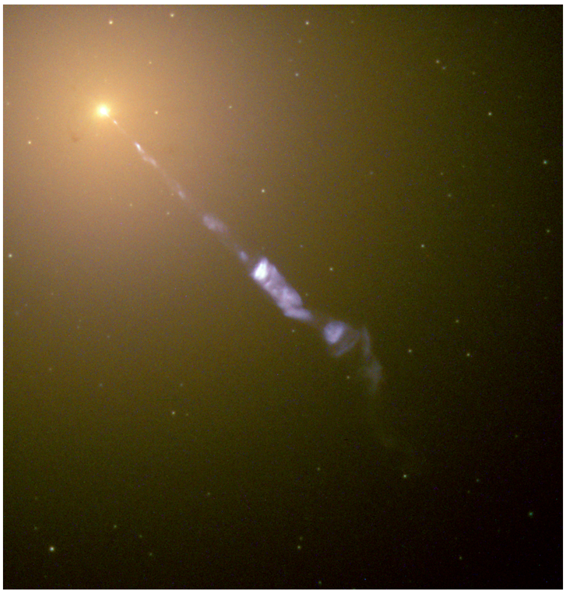

Figure 2.2: The radio galaxy Messier 87 in the optical regime, observed by Hubble Space Telescope. The long jet can be seen clearly.
(`https://en.wikipedia.org/wiki/File:M87_jet.jpg`)

Active Galactic Nuclei

Active Galactic Nuclei (AGN) are cores of galaxies that show enormous activity. These activities can have various reasons and manifestations. Sometimes the luminosity in the center of such a galaxy is much larger than that of the total rest of the galaxy. Many AGN are believed to be powered by the gravitational energy of a supermassive black hole. One subclass of them are the radio galaxies. These are, by definition, sources of powerful radio emission, which is caused by synchrotron emission from electrons ejected by the nucleus. Some of them also feature so called *jets* of relativistic particles. These are narrow lines of sources of electromagnetic radiation. They start on two sides of the core and extend far beyond the galaxy, perpendicular to the accretion disk of the central black hole (Karttunen et al. 2001). Relativistic jets can also develop shock fronts, giving rise to further accelerated, high energetic particles.
An example for a radio galaxy is Messier 87 (M87), whose jets can also be observed in the visible regime (see Figure 2.2). This particular radio galaxy is also of great interest for VHE gamma-ray astronomy due to the fact that fast variations of TeV gamma-ray flux from this source have been measured. Since these variations are in the scale of several days, they imply a very compact production region of the gamma rays, close to the dimensions of the central black hole (Aharonian et al. 2006). Future experiments like CTA with better angular resolution may help astronomers and particle physicists to further investigate this phenomenon.

2.2 Production Mechanisms of VHE Gamma Rays

Very-high energetic gamma rays can either be produced hadronically or leptonically. When accelerated protons or heavier nucleons interact with surrounding protons, photons or other matter in cosmic gas clouds, secondary neutral and charged pions can be produced. While charged pions primarily decay in two steps into electrons and (anti-) neutrinos, neutral pions decay with a probability $> 90\%$ into two gamma quanta (Lorenz & Wagner 2012):

$$\mathrm{p} + \text{nucleus} \rightarrow \mathrm{p}' \ldots + \pi^{\pm} + \pi^{0} + \ldots \text{ and } \pi^{0} \rightarrow 2\gamma;\ \pi \rightarrow \mu\nu_{\mu};\ \mu \rightarrow \mathrm{e}\nu_{\mu}\nu_{\mathrm{e}} \tag{2.2}$$

The primary leptonic generation process is inverse Compton scattering of low energy photons at VHE electrons:

$$\mathrm{e}_{\mathrm{VHE}} + \gamma_{\text{low energy}} \rightarrow \mathrm{e}_{\text{low energy}} + \gamma_{\mathrm{VHE}} \tag{2.3}$$

Both of these mechanisms produce VHE photons with characteristic energy spectra, allowing, to some extent, the determination of the originally accelerated particles.

3 Imaging Atmospheric Cherenkov Telescopes

In 1947, P. M. S. Blackett postulated that Cosmic Rays (and Cosmic Gamma Rays) and their secondary products produce Cherenkov light in the atmosphere that contributes to the night sky background light (Blackett 1948). Six years later, this was experimentally confirmed by B. Galbraith and J. V. Jelley (Galbraith & Jelley 1953). One of the first detectors was a simple construction of a search-light mirror viewed by a photomultiplier inside a trash can (see Figure 3.1). Over the years, this technique was refined and the first *Imaging Atmospheric Cherenkov Telescopes* (IACTs) were built. Today the *Cherenkov Telescope Array* (CTA) is on the verge of construction, representing the fourth generation of these detectors.
This chapter gives an introduction to the fundamental mechanisms for the observations of VHE gamma rays with IACTs.

3.1 Electromagnetic Showers

When a high energetic photon hits the Earth's atmosphere, it produces an electron-positron pair in the field of an atomic nucleus. Each of these products then loses Energy in the form of Bremsstrahlung in the fields of further nuclei, producing secondary photons. These photons again pair-produce, creating more electrons and positrons and so on. This leads to the formation of an electromagnetic cascade – an air shower (Gaisser 1991).
Such a shower can be illustrated with a toy model introduced by Heitler [1944]. The concept is shown in Figure 3.2. In this simple branching model, every particle or packet of energy is split in two after one collision length λ, so that the number of particles N at a slant depth of X is

$$N(X) = 2^{X/\lambda}. \tag{3.1}$$

Another assumption is that, at each interaction point, the energy of the original particle is equally distributed among the products. Therefore, at depth X, the energy of a particle is

$$E(X) = E_0/N(X), \tag{3.2}$$

where E_0 denotes the energy of the primary photon. The cascade continues until $E(X)$ reaches a critical energy E_c, when energy loss by ionization, Compton scattering, and collision losses becomes dominant. At this point, the shower reaches its maximum and the number of particles is

$$N(X_{\mathrm{max}}) = E_0/E_c. \tag{3.3}$$

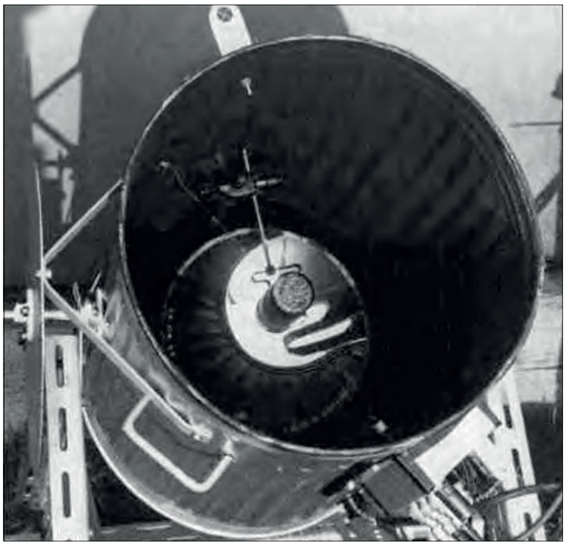

Figure 3.1: One of the first detectors for the measurement of atmospheric Cherenkov light used by Galbraith and Jelley. (`http://cerncourier.com/cws/article/cern/50222`)

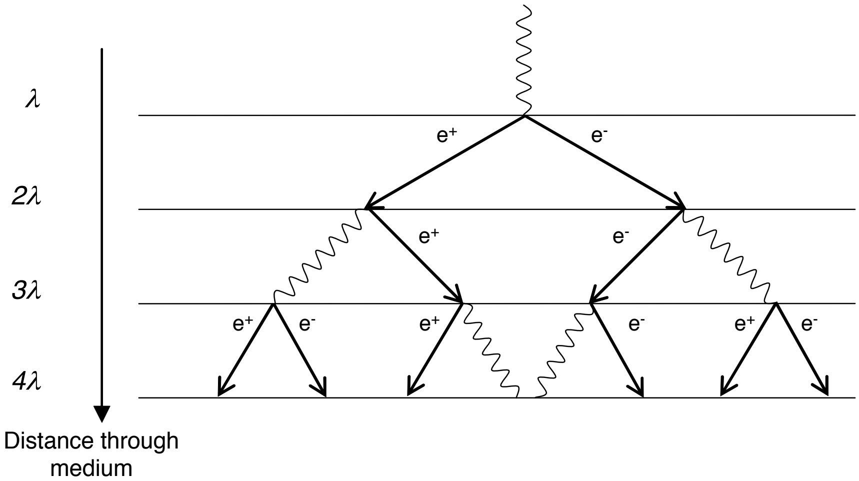

Figure 3.2: Schematic chart of the Heitler model for an electromagnetic cascade. (Lennarz 2012)

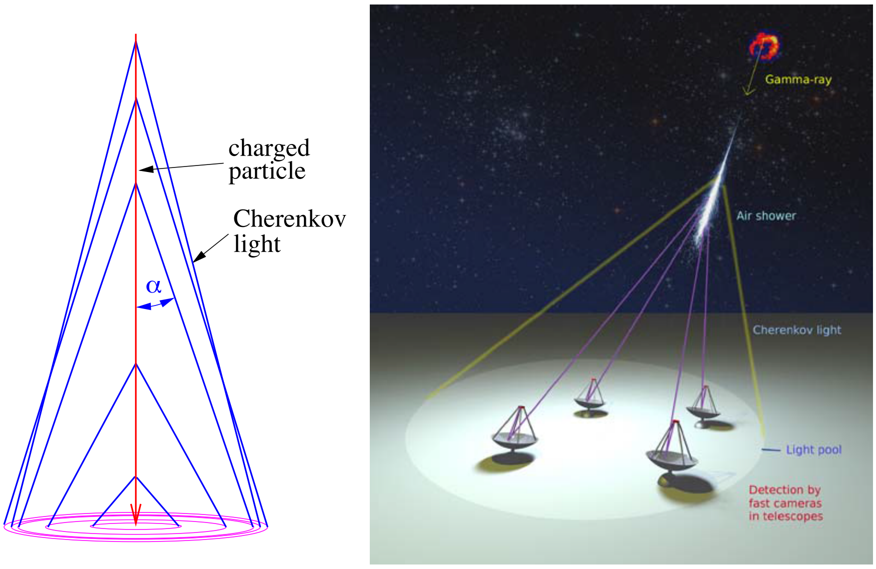

Figure 3.3: Left: Cherenkov light produced by a single, down moving particle in the atmosphere (Völk & Bernlöhr 2009). Right: Schematic view of an array of four Cherenkov telescopes in the light cone of an air shower from a gamma ray (Völk & Bernlöhr 2009).

Equating the right hand sides of 3.1 and 3.3 and solving for $X_{\max}$ yields

$$X_{\max} = \lambda \frac{\ln{(E_0/E_c)}}{\ln 2}. \tag{3.4}$$

In spite of the simplicity of this toy model, its basic features also hold for real air showers; namely

$$N_{\max} \propto E_0 \;\text{ and }\; X_{\max} \propto \ln{(E_0)}. \tag{3.5}$$

3.2 Cherenkov Radiation

As long as the velocity of a charged particle in an air shower is greater than the speed of light in the surrounding medium, the particle emits Cherenkov light. This light, which was first described by Cherenkov (1937), is created by transient polarization of atoms in the material. If the velocity is low, the polarization is symmetrically around the particle and there is no effective dipole moment. However, if the velocity of the particle exceeds the phase velocity of light, wavelets from all positions along its path are in phase, resulting in an electromagnetic wave in the far-field. Cherenkov light is radiated in a cone around the particle track (see Figure 3.3). The opening angle θ is

$$\cos\theta = \frac{1}{n\beta}, \tag{3.6}$$

where n is the refraction index of the medium and $\beta = \frac{v}{c}$ where v is the velocity of the particle and c the speed of light in vacuum. In air and for a particle with $\beta \sim 1$, this angle is about 1°. The particles in a typical air shower emit Cherenkov light that hits the ground in a circle with a radius of about 125 m (Völk & Bernlöhr 2009).

The spectrum of the Cherenkov radiation as a function of the wavelength λ can be calculated by

$$-\frac{dN}{dx} = 2\pi\alpha z^2 \sin^2\theta \int_{\lambda_1}^{\lambda_2} \frac{1}{\lambda^2} d\lambda. \tag{3.7}$$

Thereby, dx is the distance that is traveled through by the particle, $\alpha \approx \frac{1}{137}$ the fine-structure constant, and z the charge of the particle (-1 for an electron). The dependence $\frac{1}{\lambda^2}$ shows that shorter wavelengths are favoured.

3.3 Detection Principle of IACTs

Cherenkov telescopes are designed for the detection of Cherenkov light that is produced in an air shower. The challenge is to calculate the original direction and energy of the primary photon. By accumulating multiple reconstructed primary photons, sky maps and energy spectra can be produced.

Since the brightness of the Cherenkov light is very low, big mirrors are used for its collection. The light is then mapped on an array of photo sensors (see Figure 3.3). Photomultiplier tubes (PMTs) or silicon photomultipliers (SiPMs) are utilized to allow for the recording of the very short Cherenkov flashes, which are only a few nanoseconds long. These dedicated Cherenkov cameras make it possible to separate the signal from the night sky background.

The light of a particle shower produces an approximately elliptical image in a camera. If several telescopes are used to detect one shower in coincidence, the primary particle's origin can be determined by the intersection point of the major axes of the individual images (see Figure 3.4). This stereoscopic observation method also improves the accuracy of the energy reconstruction since the multiple images form a three-dimensional view of the shower, revealing also the height of the shower with the maximum particle number. This height and the total luminosity, which correlates to the total particle number, are related to the primary energy (see Equation 3.5).

3.4 Pointing and Tracking

The pointing of an IACT describes the direction the telescope is aligned to and also the ability to relate a point in the image plane of a Cherenkov camera to a position in the sky. Like optical telescopes, Cherenkov telescopes have to track sources, following their apparent movement over the sky. Due to their size and mass, and to reduce costs, IACTs typically have an azimuthal mount. Compared to equatorial mounts, where one axis of rotation is parallel to the Earth's axis of rotation, azimuthal mounts require rotations of varying speed around both axes, namely azimuth and altitude axis. This kind of tracking

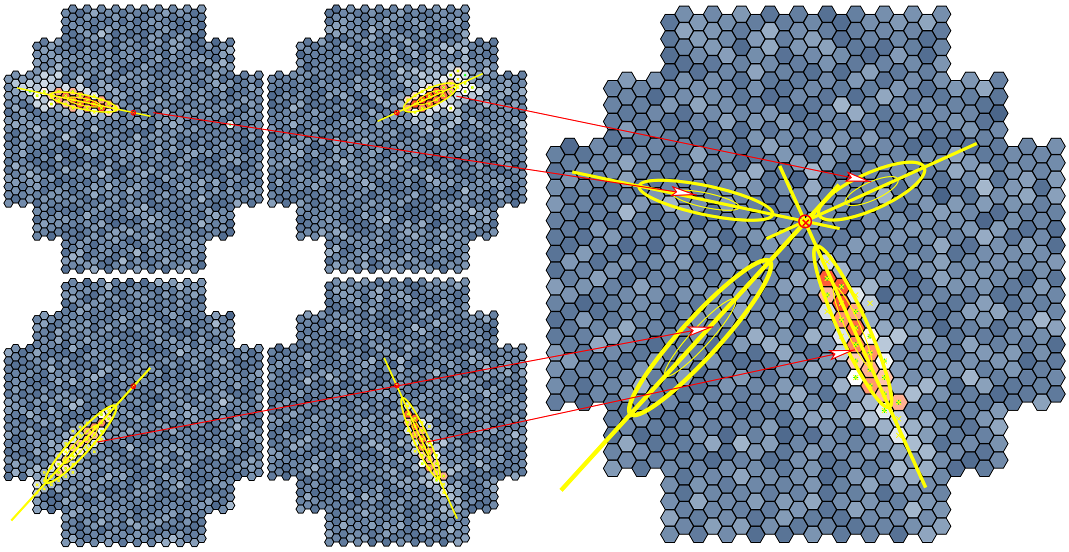

Figure 3.4: The images of one air shower taken by four Cherenkov cameras are projected into one image. The intersection point of the major axes correlates to the arrival direction of the primary photon (Völk & Bernlöhr 2009).

also leads to a rotation of the field-of view, depending on the current positioning in the sky and the geographical latitude of the telescope. The angular velocity ω of this rotation is

$$\omega = W \cdot \cos\left(\text{Latitude}\right) \cdot \frac{\cos\left(\text{Azimuth}\right)}{\cos\left(\text{Altitude}\right)}, \tag{3.8}$$

where W denotes the Earth's rotation of $4.178 \cdot 10^{-3}$ degrees per second (Keicher 2005). It is important to know the pointing of each telescope in an array as precisely as possible for the calculation of the origin of an air shower. Due to this fact, one does not only rely on the mechanics and the tracking system of the telescope. There are some mechanical effects that lead to mis-pointing, i.e. the real pointing is not as expected to be. Reasons of mis-pointing stated by Lennarz (2012) are:

- tracking offsets,
- tracking non-linearities,
- non-vertical alignment of the azimuth axis,
- offsets and rotation of Cherenkov camera,
- non-perpendicular alignment between the azimuth and the altitude axes,
- bending of telescope components.

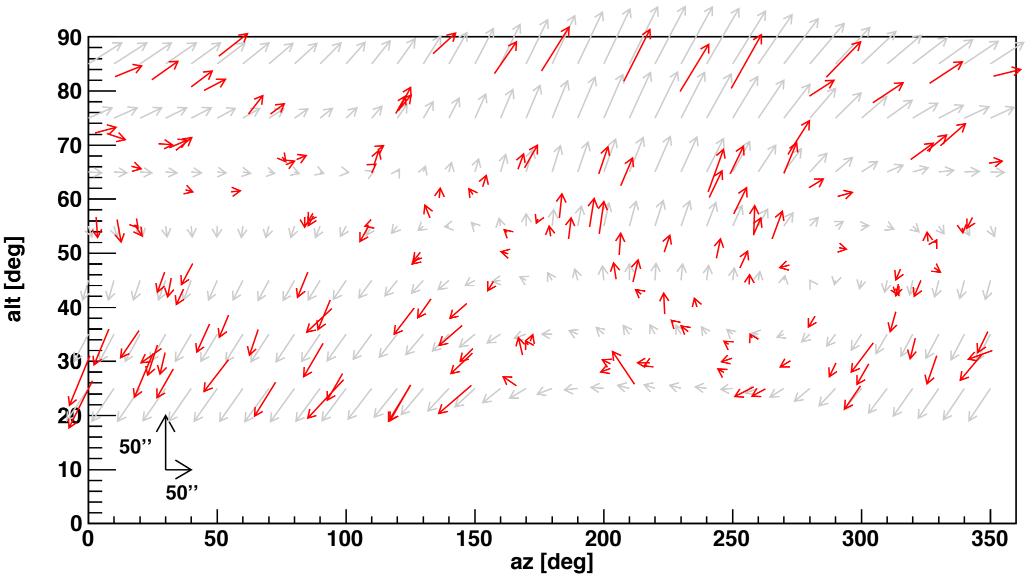

Figure 3.5: Example for a pointing model for one of the H.E.S.S. telescopes. The red arrows represent measurements of the telescope mis-pointing at the given sky-positions. Grey arrows show the pointing corrections from the fitted model. All arrows are scaled. (Lennarz 2012).

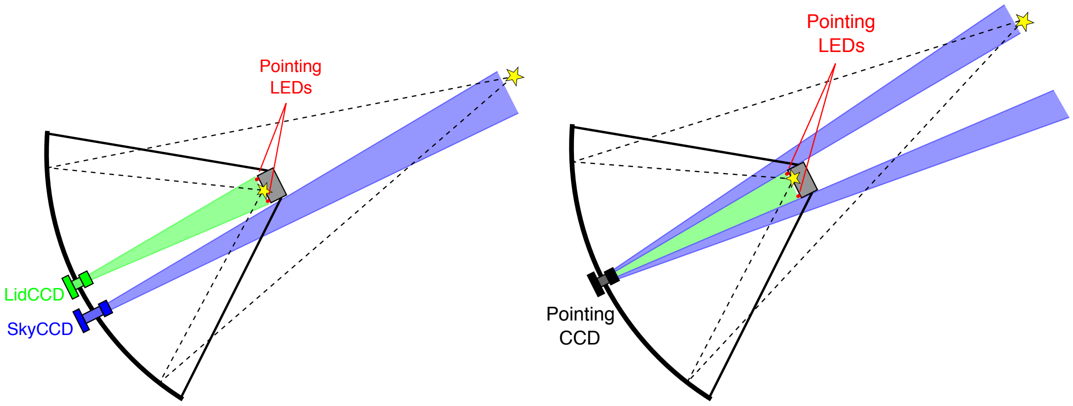

Figure 3.6: Left: Concept of LidCCD and SkyCCD mounted on a telescope.
Right: A single PointingCCD observes sky and Cherenkov camera simultaneously (Herpich 2010).

In other fields of astronomy, this pointing-problem is solved by calibrating captured images with known positions of objects in an image. This technique is called *astrometry*. It is possible for optical telescopes, but not for VHE gamma-ray astronomy because there are only in the order of 100 sources in the whole sky. So it is very unlikely that there are multiple strong, known sources in one typical field-of-view of a few degrees. The pointing of IACTs is therefore measured using optical starlight, for instance. When the real pointing is known at some different alignment directions, a mechanical model for the mis-pointing of a telescope can be fitted, which can be used to correct the pointing. The graphical representation of such a pointing model can be seen in Figure 3.5.
The following paragraphs give a short summary of how the pointing was measured for previous gamma-ray telescopes.

Pointing Runs

In the HEGRA experiment (Mirzoyan et al. 1994), dedicated pointing-runs were used to determine corrections to the pointing at certain positions in the sky-hemisphere above the telescope. The telescope was aligned to a bright star and the sky was scanned in a 2-dimensional grid around this star until the maximum in the signal of the central PMT pixel of the Cherenkov camera was found. In this position, the telescope was pointed exactly in the direction of the star. The deviation between the theoretical pointing for the star and this position of maximum current corresponded to the local pointing correction.

Standard Pointing

The H.E.S.S. experiment uses an enhancement of this method (Lennarz 2012). In pointing-runs, bright stars are mapped onto the lid of the closed Cherenkov camera. The image of the star is then captured by a CCD (charge-couple devices)-camera that is located in the center of the mirror dish. This camera is called *LidCCD* (see Figure 3.6). The mis-pointing corresponds to the offset of the star image from the lid center. This technique makes the pointing-runs significantly less time-consuming.

Precision Pointing

The H.E.S.S. Collaboration also developed a new technique for measuring pointing corrections. This technique uses a second camera, the *SkyCCD*, in addition to the LidCCD. This camera is mounted outside of the center of the dish, so that it can observe the sky next to the Cherenkov camera (see Figure 3.6). The major advantage of this configuration is that the pointing can be measured while the lid of the Cherenkov camera is open and the camera is taking data. The Cherenkov camera is equipped with several Pointing-LEDs (Light Emitting Diodes) that are imaged by the LidCCD to track its exact position. A sky-lid model calculates the positions of stars captured by the SkyCCD, as if they were mapped onto the lid. Pointing corrections derived with this technique supplement those from a pointing model and compensate short-term deformations of the telescope.

Single-CCD-Concept

The Single-CCD-Concept combines the LidCCD and SkyCCD into one *PointingCCD* with a larger field-of-view that observes both the Cherenkov camera with its Pointing-LEDs and the sky around it (see Figure 3.6). This makes an error prone sky-lid model unnecessary and saves costs and complexity by requiring only one CCD-camera. But this solution also has a few drawbacks. The first problem is that the PointingCCD can not be focused both on the Cherenkov camera (~ 30 m) and on the sky (∞) at the same time. This is overcome by focusing on the hyperfocal distance, i.e. twice the distance to the Cherenkov camera. This leads to equal defocusing of Pointing-LEDs and stars (Herpich 2010). Another problem is the reduced resolution of the sky image in comparison to the Precision Pointing technique because of the larger field-of-view.
However, due to its reduced complexity, the Single-CCD-Concept is very suitable for the several tens of medium-sized telescopes of CTA.

3.5 The Cherenkov Telescope Array

The Cherenkov Telescope Array (CTA) is an international project to build the next generation IACT for measuring very-high energetic gamma radiation. It is planned as a successor to the present instruments H.E.S.S., MAGIC, and VERITAS. It will consist of two arrays of Cherenkov telescopes, one on the northern and one on the southern hemisphere, to be able to observe the whole sky. The main site on the southern hemisphere will primarily survey the central regions of the Milky Way while the smaller northern array will be targeted especially on the exploration of AGN and star formation and evolution. The main goals that CTA aims to achieve in respect to current experiments are an increased sensitivity by one order of magnitude for observations around 1 TeV,

Figure 3.7: The prototype of a medium-sized telescope in Berlin/Adlershof. (`http://www-zeuthen.desy.de/cta\_cam/photogallery1/`)

a larger detection area and therefore higher detection rates, an increased angular resolution, a uniform energy coverage for photons from tens of GeV to beyond 100 TeV, and enhancements of the sky survey capability, monitoring capability and flexibility of operation (Actis et al. 2011). The exact layouts of the arrays are yet to be defined, but it is clear that there will be three different sizes of telescopes.

A small number of large-sized telescopes (LST) with large dishes with diameters of $20 - 30$ m will detect primarily showers from photons of < 100 GeV. Such showers emit very few Cherenkov photons, which have to be collected efficiently, but they occur at high event rates, which limits the necessary area to be covered by these telescopes.

Air showers from photons above 10 TeV appear at low rates, which requires large covered areas, but they are relatively bright and therefore do not need large mirror-dishes for their detection. These requirements are met by a large number of small-sized telescopes (SST) that are distributed over an area of multiple square kilometers.

The core energy range between 100 GeV and 10 TeV will be covered by medium-sized telescopes (MST). A prototype for one of these telescopes is currently set up in Berlin (see Figure 3.7). It has a dish frame with a maximum flat to flat diameter of 13.8 m that is equipped with a mixture of 84 real mirrors and dummy mirrors (Behera et al. 2012). The focal length of each mirror facet is 16.07 m. At this distance from the dish, a dummy Cherenkov camera is attached.

4 A Pointing Solution for the MST

The goal of this thesis is to test a Single-CCD-Concept for the medium-sized telescopes of CTA. For this purpose, a housing for an astronomical CCD-camera is developed and analyzed for its thermal properties. The following chapter deals with the details of the hardware. Chapter 5 describes a simulation software that can be used for the creation of images that are expected to be taken by a pointing-camera on an IACT. In Chapter 6 a software library is introduced that analyzes pointing-images and calculates the alignment of the camera.

4.1 Camera Hardware

A pointing-camera for a Cherenkov telescope has to fulfill several requirements. First of all, it has to be able to take pictures of the night sky and a few small LED-spots, which are both not very bright. A larger and more sensitive sensor is therefore benefiting. Colors in the images are not necessary, so the sensor can be monochrome. Since longer exposure times of several seconds are required, an active chip-cooling for reducing thermal noise is helpful. The camera must also have a digital interface so that it can be operated from the central telescope control. This connection can not be done with a USB cable, because these are limited to a length of 5 m (USB Implementers Forum 2015), which would require data processing and additional electronics close to the telescope dish. A more preferable solution would be an Ethernet connection, which allows for cables of lengths of 100 m (IEEE Computer Society 2015). Another important property is reliability. To minimize maintenance efforts, the pointing-cameras of CTA should be operational throughout the experiment's entire lifetime of 25 years, during which they will take several million pictures each. This demands a great deal of the camera electronics but also of the housing, that shields the camera from environmental damage. This damage can be caused by rain or dust. Furthermore, the environmental requirements for CTA state temperatures during observations between -15 °C and $+25$ °C and demand extremal survival temperatures of -20 °C and $+40$ °C for all components (Carr 2013). Of course the PointingCCD inside its housing also has to meet these requirements.

4.1.1 CCD-Camera

All requirements mentioned above are met by the astronomical CCD-camera Aspen CG8050-S-G01-HSH from *Apogee Imaging Systems*. It has an interline CCD-sensor that supports electronic shuttering, so the camera has no mechanical shutter, which can be affected by wear and tear. This has been a problem with another camera that has been in use earlier during the tests for this thesis, an Aspen CG8300. This first camera has a mechanical iris shutter, that ceased to function properly after several tens of shutter cycles. The shutter has been repaired by the manufacturer once, but did only work for another few shutter cycles after that. Most of the thermal optimizations of the housing described below have been done with the use of this camera. This is not a problem because the two models differ only in their sensors and the omission of a mechanical shutter. The external dimensions are the same for both cameras.

The Aspen CG8050-S-G01-HSH has a C-mount mounting for photographic objectives. This is simply a threaded hole where a lens can be screwed in.

A Peltier element is attached to the backside of the sensor, which itself is connected to a heat sink. This heat sink is ventilated by two fans. In this original configuration, the CCD-chip can be cooled to a maximum of 60 K below ambient temperature. The technical specifications state an operating temperature between -20 °C and $+40$ °C.

The camera comes with an external 12 V power supply that is connected via a coaxial power connector. It has both an USB 2.0 and a 2 MHz Ethernet interface with a built-in web server. For the communication with the camera, the software library *libapogee* (version 3.0.3179-Fedora21-x64) is used on a Scientific Linux (version 6.6) virtual machine. More technical details can be deduced from the data sheet in Appendix A.

4.1.2 Sensor

The camera uses an interline Kodak KAI-08050 sensor. This monochrome sensor has a resolution of (3298 x 2472) pixels at an active image size of 18.13 mm x 13.60 mm. It supports electronic shuttering, which means that an image can be read from the chip while the sensor is exposed to light. This is done via opaque strips that are located between columns of photosensitive pixels. During the readout, the collected photoelectrons are shifted into these strips at once and are collected from there. Due to these strips, the photon sensitivity of such an interline CCD is poor compared to Full Frame chips, which pass the photoelectrons directly on between the photodiodes and therefore have a bigger sensitive area. This can partly be compensated by the use of microlenses, that focus light from a bigger area on one photodiode (Hamamatsu Photonics K.K. accessed October 11, 2015). The datasheet in Appendix B shows more technical details about the CCD-sensor.

4.1.3 Photographic Objective

The applied objective is a Nikon AF NIKKOR 50 mm f/1.8D. Its optics consist of 6 elements in 5 groups and it has almost no distortion. It has a fixed focal length of 50 mm and its aperture allows for focal ratios (f-numbers) between 1.8 and 22 in eight discrete steps. The lens has a Nikon F-mount, a standard bayonet joint for Nikon cameras, which can be attached to the C-mount of the camera via an adapter. This adapter moves the objective further away from the CCD-sensor, so that the marks on the focus ring do not represent the real object distances. The focal length of 50 mm results in images with a theoretical opening of $20.52° \times 15.47°$ if there was no adapter between lens and camera. With this adapter, the real opening angles are slightly smaller. The opening is equivalent to a plane of 5.79 m × 4.35 m parallel to the sensor at a distance of 16 m if the objective

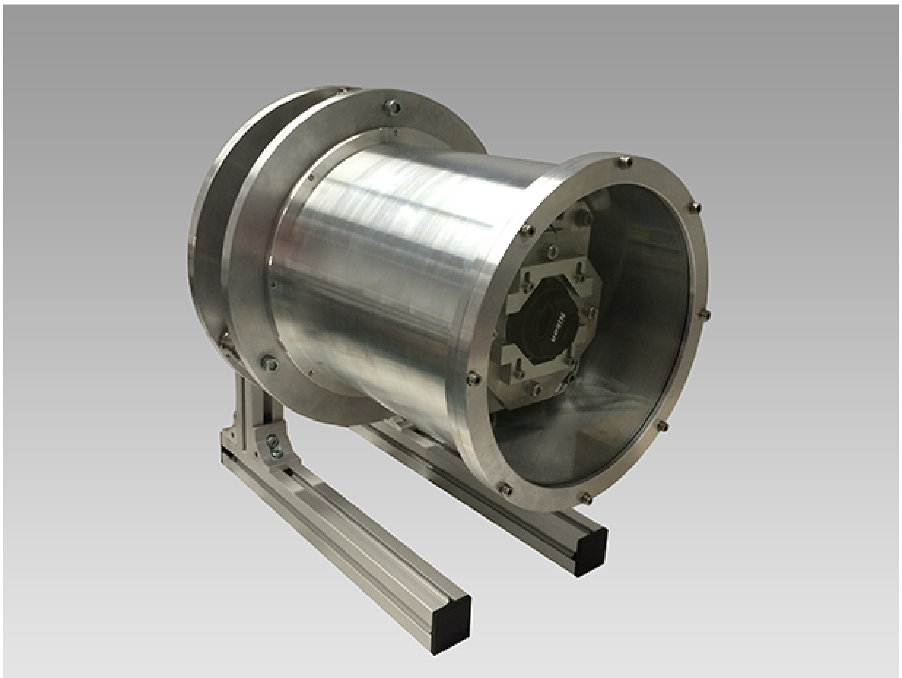

Figure 4.1: The first housing prototype for the PointingCCD. The lens cap of the camera can be seen behind the glass front plane.

is focused on a distance of 32 m. So a Cherenkov camera with a typical edge length of 3 m occupies about 36% of an image.

4.2 Development of a Housing

The housing for the CCD-camera has two primary functions: It has to protect the camera from environmental impact like water and dust, and it has to provide a rigid support which can be attached to the telescope dish so that the camera can not move relative to the telescope. The starting point for the development of such a housing is a composition similar to the one used by Lennarz (2012) for the PointingCCD during the testing of the Single-CCD-Concept at the H.E.S.S. telescopes. In this first Prototype, the complete camera is mounted on four steel rods inside an aluminum cylinder with a glass front plane. For easier handling in the laboratory, the housing is attached to two feet made of two all-aluminum construction rails each. These rails are joined together with two elbow connectors each and make it possible to arrange the housing horizontally. The construction can be seen in Figure 4.1.

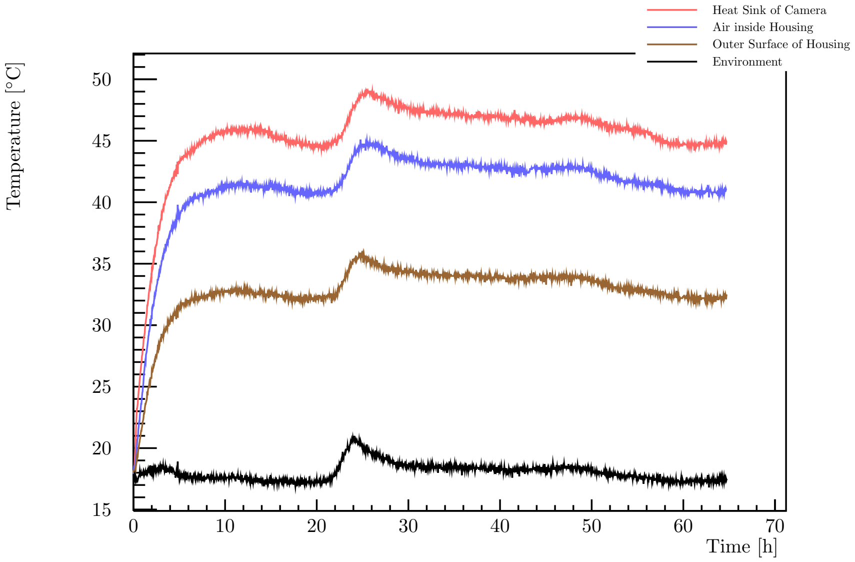

Figure 4.2: Measurement of temperatures at different locations in the first prototype of the camera housing with the first camera Aspen CG8300. At 0 h, when all parts of the structure have the environmental temperature, the camera is switched on. At approx. 22 h, the sun heats the laboratory.

4.2.1 First Prototype

To maximize the lifetime of the CCD-camera, it is desirable that the air inside the housing does not exceed the maximum operating temperature of the camera. For this purpose, a test setup is established. A program simulates an operation of the camera on a telescope during observation. Therefore an image is captured every minute for the duration of one hour. After that, a period of another hour follows, in which no images are taken. Then another hour with captured images follows, and so on. During this time, the CCD chip is constantly cooled to −10 °C and the two fans of the camera circulate at maximum speed. This temperature is chosen because it is slightly lower than −5 °C, which has been determined as an optimal working temperature for the Aspen CG8300 by Specovius (2014). If the housing can dissipate the heat from a Peltier element that cools to a lower temperature, it can also dissipate the heat from an element that uses less power. A data logger (Voltcraft PL-125-T4USB VS) records the current temperatures at four different spots every two minutes: one temperature-sensor is placed in the interior air in front of the objective, one on the heat sink of the camera, one on the outer surface of the housing cylinder, and one sensor is thermally decoupled from the setup for the observation of the environmental temperature. The trend of these temperatures over 64 hours can be seen in Figure 4.2. It is obvious that the temperature inside the housing exceeds the operating temperature of the camera of 40 °C even though the environmental temperature is below the maximal operating temperature of CTA of 25 °C. This high

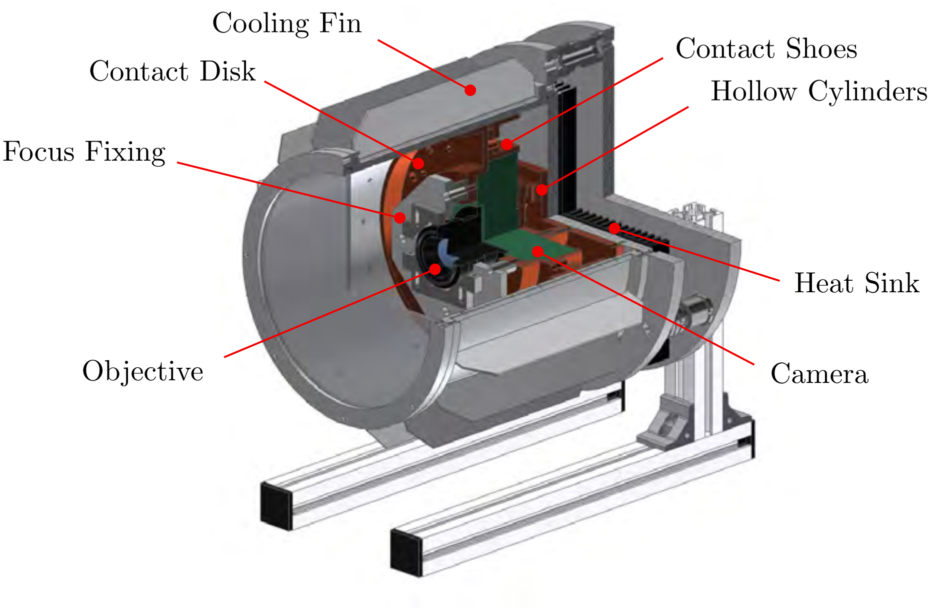

Figure 4.3: Optimized prototype of the camera housing by Hofmann (2015).

internal temperature arises from the fact that the heat which is produced by the camera is transferred very inefficiently out of the housing. Besides the four steel rods, the camera is coupled thermally to the outside only over the interior air.

4.2.2 Optimization of Thermal Conductivity

P. Hofmann investigated the thermal properties of this prototype in more detail in his bachelor thesis (Hofmann 2015). This thesis originated as a spin-off of the present thesis. The goal was to seek possibilities to improve the thermal conductivity of the housing, so that the camera's operating temperature is not overshot. To achieve this goal, the heat transmission over air was replaced by heat transmission over metal as far as possible. This was done on a successive development basis with several steps. Here, only the final configuration is presented.

The optimized prototype is sketched in Figure 4.3. Heat sink and fans of the camera Aspen CG8300 were demounted and replaced by two interlocking copper hollow cylinders. One cylinder has been attached to the warm side of the Peltier element, a spot on the camera where a lot of heat is produced. The other hollow cylinder has been connected to the backplate of the housing. To the outer side of the backplate, a passive heat sink has been attached, that increases the surface of the backplate and generates thermal convection. The front and sides of the camera have been connected to the side surface of the housing cylinder via a copper disk and three copper shoes respectively. Sixteen

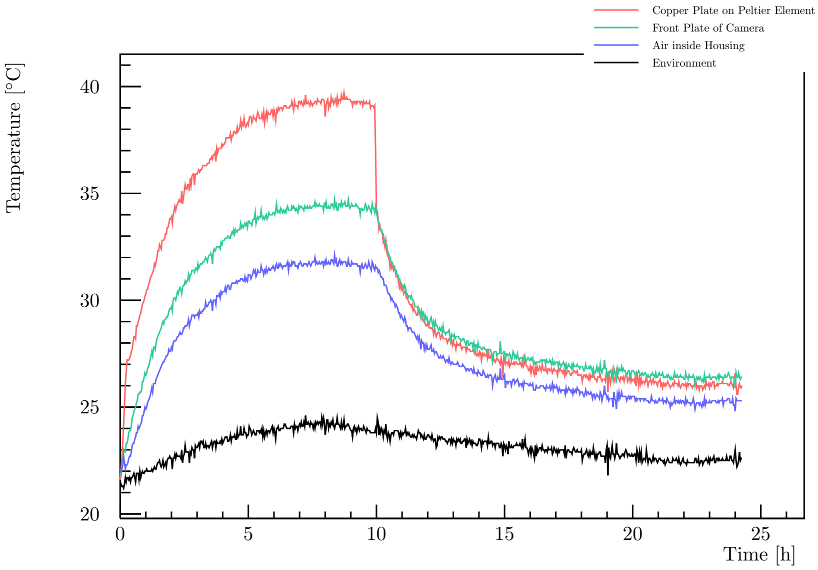

Figure 4.4: Measurement of temperatures at different locations in the optimized prototype of the camera housing. The new camera Aspen CG8050-S-G01-HSH is used for this test. At 0 h, when all parts of the structure have environmental temperature, camera and chip cooling are switched on. At 10 h camera returns to stand by.

all-aluminum cooling fins have been attached to the outer surface of the cylinder. In addition, heat-conductive paste has been applied to important transition points between different components.

With all these changes to the original design (except the copper shoes, which were not yet available at that time), the heat conduction of the housing could be enhanced insofar as that the temperature inside the housing reaches only 31.8 °C at an environmental temperature of 22.2 °C. With this difference of 9.6 K, the CCD-camera should be able to work below its maximum operating temperature at a surrounding air temperature of 25 °C.

The thermal conductivity of the housing is also measured with the new camera Aspen CG8050-S-G01-HSH. This time, the copper shoes are also integrated. Figure 4.4 shows the temperatures at different locations in this installation. For the first ten hours, the camera operates as described in Section 4.2.1. After that, the chip cooling is turned off and the camera changes into stand by. The air temperature inside the housing reaches a maximum of 32 °C at an environmental temperature of 24 °C. The thermal difference of 8 K proves, that the copper shoes can improve the thermal conductivity of the housing.

4.2.3 Further Improvements to the Housing

Although the thermal conductivity of the housing seems to be sufficient to keep the camera within its operating temperature range, further enhancements are necessary for the small volume production.

The current prototype has a mass of 27.5 kg whereof 10.3 kg is copper. If the copper elements could be replaced by aluminum, which has about one third of the density of copper (The Engineering ToolBox 2015) and costs about one third less per kilogram (finanzen.net 2015a,b), weighting and expanses could be reduced. However, this will also affect the thermal properties of the housing because of the lower thermal conductivity of aluminum. The factor is heavily dependent on the purity of the deployed alloys. It still has to be investigated if such a replacement is reasonable.

Another problem that has to be solved is the cable feedthrough for power and Ethernet. In the current prototype, this has been accomplished by Hofmann (2015) simply by a hole, that is big enough for an 8P8C plug. Both cables are pushed through this hole and silicone is used to seal it. This is satisfactory for temperature measurements in the lab, but not for long-term use. Possible solutions could be the use of weather-resistant sockets and plugs on the outside or air-proof cable feedthroughs.

Last, it should be checked if the cylinder can be shortened, which would save material. The current mount inside the housing fixes the camera closer to the backplate than in the first prototype. This generates a lot of unused space between the objective and the glass plate. The drawback of a shorter housing would be a reduced surface, which goes along with worse thermal conductivity.

4.3 Summary

In this chapter, an astronomical CCD-camera and a lens have been introduced, that are applicable as a Single-CCD pointing solution for an IACT. The development of a housing with regard to its rigidity and thermal conductivity has been described. It has been shown that the current prototype meets most of the requirements for an application on a telescope. The chapter closes with the discussion of further necessary steps for the hardware development.

5 Simulation and Analysis of Pointing Images

In order to simulate images that can be captured by a pointing camera that is mounted to a Cherenkov telescope, a software library named `libCCDCamera` is developed. This software is written in `C++` and links against the H.E.S.S. Analysis Pipeline (HAP) software in the version 13-06 and `ROOT`, a data analysis framework developed at Cern, in the version 5.34.18. The starting point of `libCCDCamera` has been received from internal communications and is refined in the framework of this master's thesis.

An image is produced in three basic steps: At first, star positions are retrieved from a catalogue. Then, the sky-coordinates of the stars are transformed into pixel-coordinates on the virtual CCD-chip. Finally, a two-dimensional histogram, that represents the image, is filled with a two-dimensional Gaussian distribution at the calculated coordinates for each star in discrete time-steps, which add up the complete exposure time. The following chapter starts with a detailed description of these fundamental steps.

The primary challenge for analyzing pointing images is to recognize star constellations in the image and to set up a transformation between pixel coordinates and astronomical coordinates. The necessary calculations are implemented in the open source software `Astrometry.net`. One of the main goals of this thesis is to test, whether this software is suitable for calculating pointing corrections for Cherenkov telescopes.

In the second half of this chapter, `Astrometry.net` and its functional principle are presented. Then, a wrapper library that simplifies the use of the open source software and that could serve as an interface to further CTA software is introduced.

5.1 Parameters and Classes

The simulation consists of five major classes: The main class `Exposure` represents a simulated image. It comprises essential parameters like the start time, the exposure time, and the observation direction. The size of the time-steps is also defined in this class. It can also be stated whether the dummy Cherenkov camera, which is defined in the referenced `CherenkovTelescope` object, should be drawn in the picture. This is currently a rectangle with arbitrary edge lengths in the center of the image that blanks the light of all stars in that region. Furthermore, the visibility of stars below the simulated horizon can be toggled.

The class `CherenkovTelescope` implements the properties of the virtual Cherenkov telescope. Those properties are the focal length of the telescope, the size of the Cherenkov camera, and the positions of optional Pointing-LEDs on the latter. These LEDs are re-

presented by the class `Marker`.
All characteristics of the virtual PointingCCD are stored by the class `CCDCamera`. This includes the focal length, focal distance, and aperture of the objective and the dimensions, temperature and quantum efficiency of the sensor. There are also several subclasses for particular CCD-cameras, that have been in use. The fifth class, `Geometry`, implements all coordinate transformations of the simulation (see Section 5.3).
An UML (Unified Modeling Language) class diagram of library with the most important parameters and methods is shown in Appendix C.

5.2 Star Positions

Star positions are retrieved from a `Crash::SkyMap`, a class of the H.E.S.S. software, that uses the Tycho-Catalogue. The star data includes coordinates in the `RADecJ2000`-System and apparent magnitudes. A limit to the apparent magnitude can be set here to reject stars that are too faint to be visible in the image.

5.3 Coordinate Transformations

All coordinate transformations that are used in the simulation are implemented by the H.E.S.S. software. These transformations are described in great detail by Gillessen (2004). An overview of the coordinate systems used for the simulation is given below.

Equatorial Systems

The `RADecJ2000System` is a spherical, two-dimensional system that is used to describe the positions of celestial objects in the sky. The first coordinate, the *right ascension*, denotes the angular distance to the vernal equinox parallel to the celestial equator. The distance to the celestial equator is denoted by the *declination*. Coordinates in this system are independent of the position on Earth of the observer and, to first order, of the time. Small changes over time are caused by precession and nutation of the earth or parallax motion of the stars. Therefore celestial positions are reported for a fixed point in time. Such a point in time is called an *epoch*. The current epoch is J2000.0, which corresponds to 2000 January 1 11:58:55.816 UTC.
The `RADecTopoSystem` is a helping system, that represents equatorial coordinates on the earth's surface at a certain location and time.

Horizontal Systems

The `AltAzSystem` describes positions in the sky above an observer at a certain location on Earth with two spherical coordinates, namely *azimuth* and *altitude*. The azimuth is the angular distance to the local meridian parallel to the horizon. It is measured starting in the North in eastern direction. The altitude denotes the height above the horizon.

Coordinates in the `RADecTopoSystem` are transformed into this system via a rotation matrix.
The `HorizonSystem` is similar to the `AltAzSystem` except for its consideration of atmospheric refractions. These refractions let stars appear higher in the sky than they would if there was no atmosphere.

Telescope Systems

The `GroundSystem` is a three-dimensional, cartesian coordinate system whose origin is on the ground in the center of the telescope (in the center of the H.E.S.S. telescope array). The x-axis points to the north, the y-axis to the west, and the z-axis points upwards.
The axes of the `TiltedSystem` are equal to those of the `GroundSystem`, but they are tilted with the telescope, so that the z-axis matches the pointing direction. If the telescope is aligned to an azimuth of 0° and an altitude of 90°, the two systems are equivalent. A vector in the `GroundSystem` can be transformed into the `TiltedSystem` by two consecutive rotations.
The `NominalSystem` is a two-dimensional, cartesian coordinate system, that represents points in the focal plane of a theoretical telescope with a focal length of 1 m. The transformation from the `TiltedSystem` to this system is a simple projection:

$$\vec{x}_{\mathrm{N}} = \begin{pmatrix} -x_{\mathrm{T}}/z_{\mathrm{T}} \\ -y_{\mathrm{T}}/z_{\mathrm{T}} \\ 0 \end{pmatrix} \tag{5.1}$$

Another helping system is the `MirrorSystem`. This system simply flips the y-coordinate and is necessary in the simulation to convert left-handed coordinates of the `AltAzSystem` to right-handed coordinates of the CCD-camera systems.

Camera Systems

The H.E.S.S. software also implements the class `CameraSystem`. This system is intended for representing positions in a focal plane of the telescope. Coordinates in the `NominalSystem` transform to this system via shifting, rotating, and scaling. Three instances of this class are used in the simulation:
The `TelCameraSystem` represents positions in the focal plane of the Cherenkov telescope, i.e. on the Cherenkov camera. This system is used for mapping the dimensions of the Cherenkov camera and the Pointing-LEDs.
The `CCDCameraSystem` is used for positions on the chip of the CCD-camera. The scale factor in respect to the `NominalSystem` matches the focal length of the camera-objective. Its origin corresponds to the observation direction and positions are measured in meters on the chip.
For real pixel coordinates, the `CCDPixelSystem` is used. This system is scaled with the number of pixels per meter on the chip in respect to the `CCDCameraSystem`, rotated by 90° so that the x-axis points to the right and the y-axis to the top, and shifted so that the origin is in the bottom left corner of the chip.

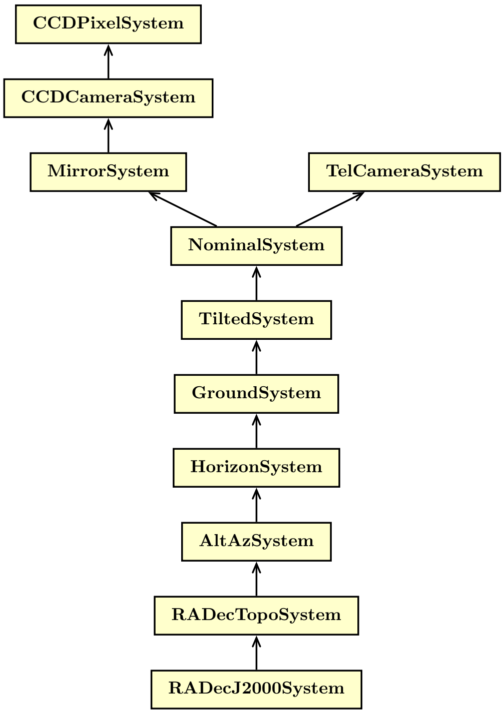

Figure 5.1: Tree of coordinate systems used in `libCCDCamera`. Each arrow represents an implemented transformation between two systems.

Coordinate Tree

The relations between the coordinate systems described above form a simply connected tree, which is sketched in Figure 5.1. The transformations and inverse transformations between any two directly connected systems is defined. This means that a position that is known in any coordinate system can be mapped to any other system in the tree. For the simulation of an image, the positions of the stars, which are defined in the `RADecJ2000System`, are mapped onto the virtual chip by a transformation into the `CCDPixelSystem`.

5.4 Filling the Histogram of the Exposure

An image is represented by a two-dimensional histogram, whose binning corresponds to the pixels on the camera sensor. To simulate the apparent movements of the stars and effects that arise from the tracking of this movement, the total exposure time is subdivided into several steps. At each time-step, the telescope is aligned to the original RA/Dec position, the stars are mapped into the `CCDPixelSystem` and a two-dimensional Gaussian distribution is added to the histogram for each star. This distribution has the

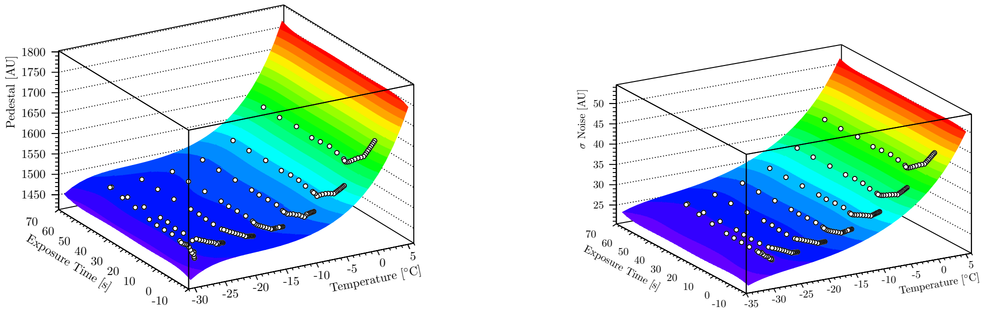

Figure 5.2: Measured pedestal and thermal noise of the Aspen CG8050-S-G01-HSH for different chip temperatures and exposure times (white circles). The colored surface represents a 2-dimensional, polynomial fit of order 5. Left: Pedestal. Right: Thermal noise.

form

$$f(x,y) = \frac{n_{\mathrm{Ph}} \cdot \epsilon}{2\pi\sigma^2} \exp\left(-\frac{(x-x_0)^2 + (y-y_0)^2}{2\sigma^2}\right), \tag{5.2}$$

where

$$n_{\mathrm{Ph}} = j \cdot A \cdot \Delta t \tag{5.3}$$

is the number of photons of a star mapped to position (x_0, y_0) with a flux j on an aperture with area A in a time-step with a length of Δt. The flux is calculated by the H.E.S.S. software, using the apparent magnitude of the star. ϵ is the efficiency of the camera system, which depends on the quantum efficiency of the chip and the imaging properties of the lens. This factor is derived from actual images of the night sky taken with the camera. For the set up described in Chapter 4, it has a value of 2.9%. The pixel-scaled circle of confusion at distance z is calculated as

$$\sigma = d \cdot \frac{|z - z_{\mathrm{f}}|}{z} \cdot \frac{f}{z_{\mathrm{f}} - f} \cdot \frac{\kappa}{s}, \tag{5.4}$$

where d is the diameter of the aperture, z_{f} the focal distance, f the focal length and s the edge length of a pixel on the chip. By the scale factor κ, the width is calibrated with images taken with the real-world instrument. It has a value of 1.85. The Gaussian distribution is evaluated at the center of each pixel for a star at position (x_0, y_0). This is done cyclically outwards from the star position until all pixel values in a circle are below the resolution of the chip. Optional Pointing-LEDs are added to the histogram in the same way.

After all time-steps, a Gaussian distributed random number is generated for each pixel and added to the histogram. This distribution uses the pedestal of the chip as its mean and the thermal noise as its standard deviation. Values for these parameters have been obtained by taking dark-frames with different exposure times at different CCD-

Figure 5.3: A simulated pointing image with the center at (RA, Dec) = (12 h 30 min 49.4 s, $+12^\circ\ 23'\ 28.0''$), the coordinates of M87. The image is simulated with an exposure time of 10 s and an f-number of 1.8.

temperatures. The parameters are taken from a polynomial fit function (see Figure 5.2).

5.5 Output and Performance

The computation time of pointing image scales linearly with the number of stars in the field-of-view and the number of time-steps. A typical image with stars with magnitudes up to 8 and 100 time-steps is simulated in the order of 10 s.
A simulated image can be retrieved from an `Exposure` instance as a `ROOT` histogram `TH2F`. The library also supports the saving in the *Flexible Image Transport System* (FITS) format. An example of a simulated image can be seen in Figure 5.3.
It is also possible to retrieve a list of the exact star positions on the virtual CCD-chip.

5.6 Astrometry.net

`Astrometry.net` is an open source software package that has been developed by Lang et al. (2010) and is mainly written in `C`. The downloadable software package contains the source code for several binaries, that are ready-to-use for image calibration, but also the source code for the binary library `libastrometry`.

The astronomical calibration that is done by `Astrometry.net` can be divided into four main steps. In the first step, stars in a given image are detected. The positions of the stars are retrieved by a number of image-processing steps to sub-pixel accuracy. In the second step, subsets of three or four stars are generated. These subsets are hereafter called "quads" and the number of stars in a quad is called the "quad-dimension". For each quad, a geometric hash code is derived that describes the relative positioning of the stars in the quad. For each hash code, the software searches for almost identical hash codes in large, pre-computed indices. Such an index is contained in a so-called "index file" in the FITS format. This search represents the third step. It is done for the whole index, so no information about the approximate alignment of the image is needed. If a match is found, a hypothesis that the quad in the image corresponds to the quad found in the index is generated by matching the remaining stars in the image with other stars in the index. In the last step, each hypothesis is tested against a null hypothesis. If a hypothesized alignment does not pass this verification, a new quad is selected and the calibration continues with step three. This is done until one hypothesis is accepted, all possible quads have been checked, or a specified time limit is hit.
If a match is accepted, `Astrometry.net` provides a *World Coordinate System* (WCS) and suitable functions, that allow for the transformation of any pixel position in the image to RA/Dec coordinates and vice versa.

5.7 Wrapper Library

In order to use `Astrometry.net` efficiently together with `ROOT` and the H.E.S.S. software, a `C++` wrapper library named `libPointingMST` is developed. This library links against `libastrometry` and currently consists of one class, the `PointingImage`. This class can be instantiated either with an image in the FITS format or with a list of known source positions and the dimensions of an image. The latter is useful for quality tests with simulated data in order to bypass the image processing algorithm. There is one method that extracts the source positions from a given image. Another method then does the reconstruction of the pointing. After that, methods that transform coordinates between the pixel system and the RA/Dec system can be used. Figure 5.4 shows an image analyzed with `libPointingMST`. The positions of detected stars and stars that have been matched with stars in the index are marked. The used quad is also shown in the image.

5.8 Outlook

The wrapper library `libPointingMST` together with `libastrometry` is suitable for studying properties and errors of the astronomical calibration of pointing images as it is done in the following chapters of this thesis. It is not applicable for long term use as part of the software for an IACT at the time when this thesis is compiled. There are still issues like huge memory leaks that make a program occupy several gigabytes of memory after the analysis of a few tens of images. `Astrometry.net` also crashes occasionally due to a segmentation fault. These errors necessitate the adoption of an executable that analyzes

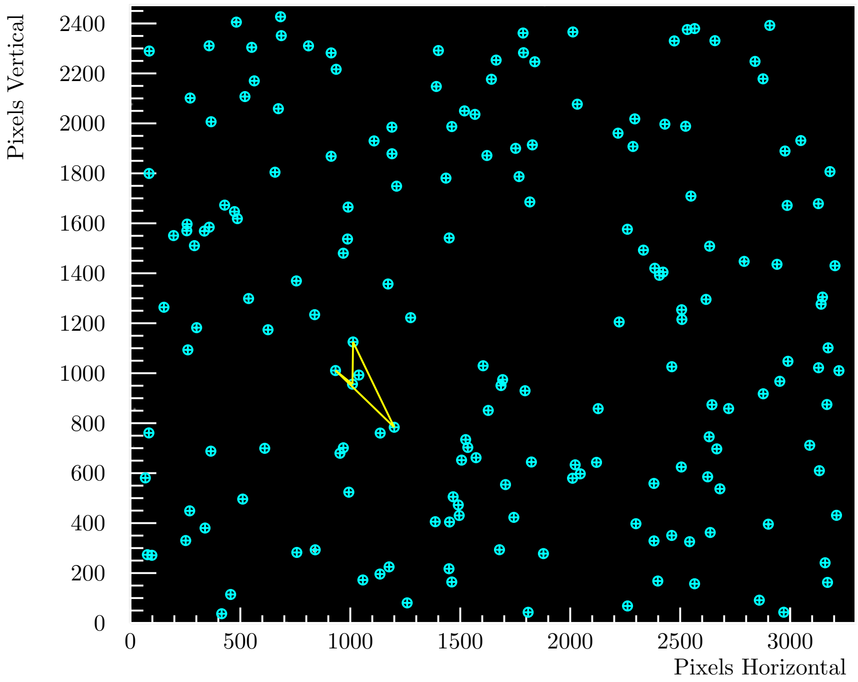

Figure 5.4: The analyzed image of the position of M87 shown in Figure 5.3. Cyan plus signs represent positions of extracted sources. Circles mark sources that have been matched with stars in the index. The used quad is indicated by yellow lines.

one image and then exits. Such an executable is then run frequently for the calibration of a set of images.
These errors are not acceptable for production software and have to be eliminated. This may include a debugging of `Astrometry.net` or its complete reimplementation and is therefore not done in the context of this master's thesis due to time limitations.

5.9 Summary

In this chapter, a software library has been presented, that allows for the simulation of pointing images as they can be captured with a CCD-camera mounted on a Cherenkov telescope. Furthermore, the open source software `Astrometry.net` has been introduced and the development of a `C++` wrapper library has been described.

6 Towards a Verification and Validation of Pointing Reconstructions

As indicated above, it is crucial that pointing images are calibrated as precisely as possible. The Guidelines for CTA Pointing Calibration demand an average uncertainty of less than $5''$, while the goal precision is $3''$ (van Eldik et al. April 2015). In order to investigate the precision of `Astrometry.net` and the wrapper library, a script is written that simulates images with `libCCDCamera`, analyses them with `libPointingMST` and relates the calculated pointing to the parameters of the simulation. In this chapter, the precision of the pointing reconstruction is investigated and its dependencies on different parameters are discussed.

6.1 Test of the Algorithm

At first, it has to be proven whether the astronomical calibration works precisely and reliably if star positions in an image are known exactly. Therefore, 10000 images are simulated at randomly chosen Alt/Az positions. These positions are isotropically distributed over the hemisphere above the virtual telescope. The chosen location for the telescope is at the coordinates of the observatory *Dr. Karl Remeis-Sternwarte* in Bamberg (49.88456° N 10.88780° E). All exposures start at 2015-01-30 23:00:00 UTC. In this first test, only the positions and luminosities of stars on the chip are passed to `libPointingMST`. So parameters like f-number or exposure time are redundant. For convenience, such a simulation is hereafter called “star field”. When the calibration is done, the center of a simulated star field is calculated and the difference to the original pointing position (the reconstruction deviation) is determined. This distance is calculated as the angular distance on the great circle, i.e. the shortest connection between two points on a sphere. If the pointing reconstruction was perfect, this distance would be zero for all simulated star fields. The actual distribution of the deviations is plotted in Figure 6.1. The largest fraction of about 96% of all star fields is calibrated with a precision of two arcseconds or better. All remaining reconstruction deviations form a separate distribution around 0.1 degrees. It is not yet fully understood, why these star fields are reconstructed with such a poor precision. The drop in precision correlates strongly with a drop in the fraction (matched stars/stars in field of view). This correlation is plotted in Figure 6.1. By means of this fraction, the two classes of hereafter called “good” and “bad” calibrations can be separated even if the actual pointing is unknown.

Another way to suppress the right part of the distribution, is to increase the critical value of log odds above which a pointing calibration is accepted. The log odds denote the log-

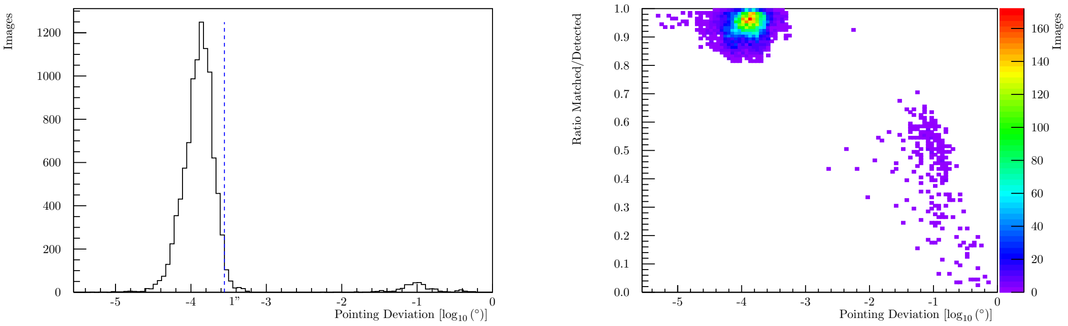

Figure 6.1: Left: Distribution of pointing deviations for 10000 simulations of star positions. Right: Correlation between pointing deviation and the quotient of matched stars over the total number of stars.

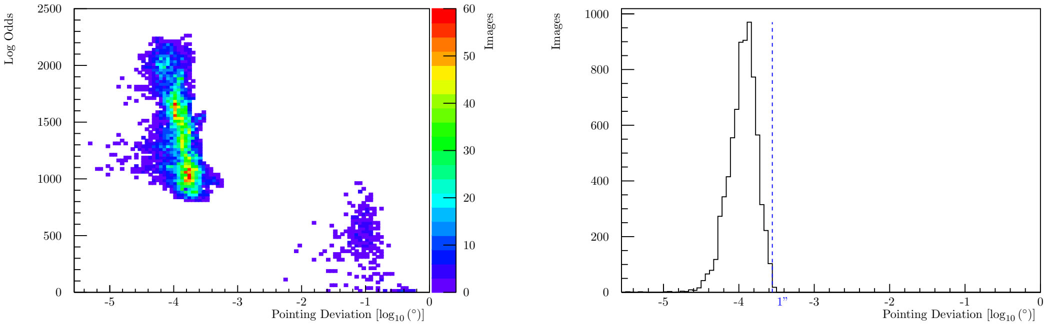

Figure 6.2: Left: Correlation between pointing deviations and log odds of accepted calibrations. Right: Distribution of pointing deviations for 10000 simulations of star positions with a critical value of log odds of 1100.

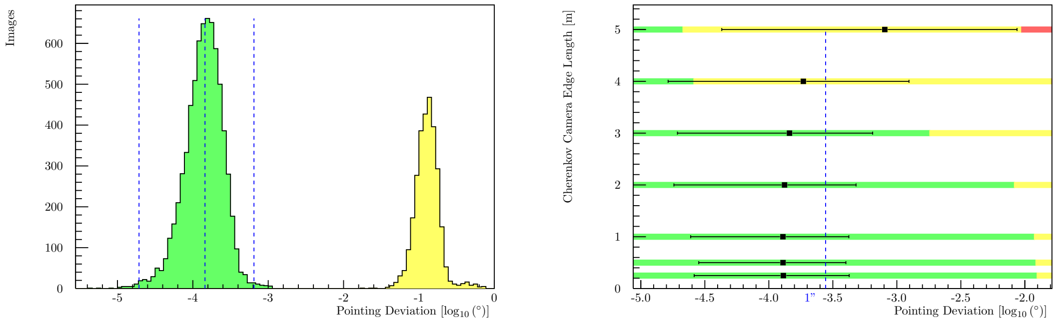

Figure 6.3: Left: Distribution of reconstruction deviations for 10000 simulated star fields with an obstructing Cherenkov camera with an edge length of 3 m. “Good” reconstructions with deviations of less than $10^{-2\circ}$ are shaded green, others are shaded yellow. The median of “good” calibrations and the interval, within which 99% of these calibrations are contained, is indicated with blue lines. Right: Medians of distributions of reconstruction errors for different Cherenkov camera sizes (black squares). The black lines indicate intervals in which 99% of the “good” reconstructions are contained. The lengths of the green and yellow bars represent the ratio between “good” and “bad” reconstructions. Red bars indicate star fields which can not be calibrated at all.

arithmic ratio of the probability that the calibration is correct to the probability that the alignment is false. The default value in `Astrometry.net` is $\ln(10^9) \sim 21$. The correlation between log odds of accepted calibrations and reconstruction deviations is plotted in Figure 6.2. Since all “bad” reconstructions have log odds of less than 1100, another set of 10000 star fields is simulated and reconstructed with this value as a lower limit. The resulting distribution of pointing deviations is plotted in Figure 6.2. In contrast to the previously discussed calibrations with the default value for minimal log odds, where all star fields can be calibrated, only about 74% of the pointing reconstructions succeed. 99.8% of the succeeded calibrations have pointing deviations of less than one arcsecond. All other succeeded reconstructions show a precision of better than two arcseconds. The downside of increasing the minimal log odds is that this dramatically increases the computation time. The 10000 reconstructions with higher log odds take about 73.5 h whereas the same number of reconstructions with default log odds only take about 10 h. For this reason, default log odd limits are used in all following studies. Nevertheless, this option should be considered when implementing production software for CTA.

6.2 Adding a Cherenkov Camera

The next question is, how a Cherenkov camera, that obstructs a certain part of the sky, influences the calibration. To investigate this influence, sets of 10000 star fields are

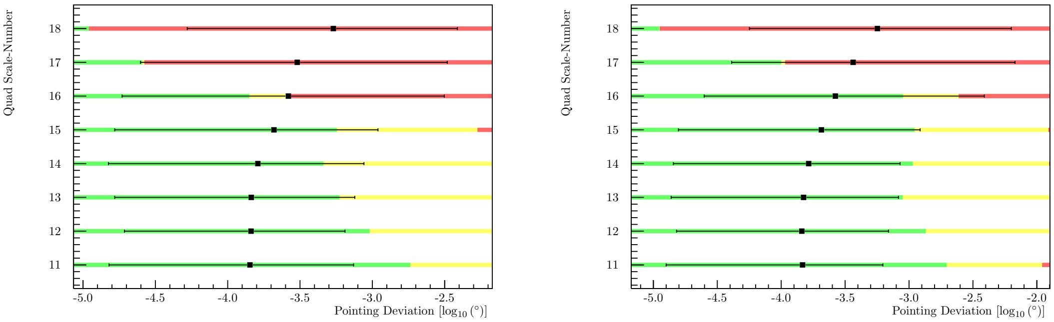

Figure 6.4: Medians and 99% containment intervals of distributions of reconstruction deviations for indices with different scale-numbers. Left: Indices with quads of four stars. Right: Indices with quads of three stars.

simulated with central, blank squares with different edge lengths. In Figure 6.3, the distribution of reconstruction deviations for a Cherenkov camera with an edge length of 3 m is plotted. This is about the size of cameras for the MST that are currently in development (Moulin et al. 2015).
Both the “good” and the “bad” sub-distributions are shifted to higher deviations in comparison to unobstructed star fields. The fraction of “bad” reconstructed star fields is also significantly larger (29%). For eight star fields, the calibration fails and no pointing can be calculated. The results for other camera sizes are also illustrated in Figure 6.3. The plot shows that the precision of the calibration starts to drop with a camera size of 2 m. From this point, the deviations are more and more shifted to higher values. The fraction of “bad” reconstructions also increases significantly. These problems arise from the fact that the algorithm that matches sources in the star field with sources in the index has fewer stars available.

6.3 Changing the Index Files

Another important parameter of the reconstruction is the choice of the index file. `Astrometry.net` works with different index files, which have different mean quad-sizes. The documentation states that this size should be 10% to 100% of the size of the images to analyze (Lang et al. 2015). The software also accepts indices with different quad-dimensions. According to Lang et al. (2010), only indices with quads of three or four stars are sensible. There are several index files available to download from the `Astrometry.net` website. The software package also contains an executable `build-astrometry-index` which can be used to produce index files. This executable takes three parameters: the path to a FITS-file that contains star positions, the quad-dimension, and the scale-number, which correlates with the quad size (see Table 6.1). For the analyses done for this thesis, index files are produced that use the same Tycho-Catalogue as the simulation and comprise stars with apparent magnitudes up to 8.

Table 6.1: Predefined scale-numbers and corresponding quad-sizes in `Astrometry.net` (Lang et al. 2015).

Scale-Number	Quad Size Range [arcminutes]
19	1400 - 2000
18	1000 - 1400
17	680 - 1000
16	480 - 680
15	340 - 480
14	240 - 340
13	170 - 240
12	120 - 170
11	85 - 120
10	60 - 85

To investigate how the choice of the index file affects the quality of the reconstruction, one set of star fields is simulated and analysed for each scale-number, once with a quad dimension of four and once with a quad dimension of three. All star fields are simulated with a Cherenkov camera with an edge length of 3 m. The characteristics of the resulting distributions of pointing deviations are plotted in Figure 6.4. Only indices with the shown scale-numbers can solve the simulated star fields. Index files with a scale-number of 19 have quads with sizes of more than 23°, which can not be contained in one image. This problem begins to show starting at a scale-number of 15. From this point, the fraction of unsolvable star fields increases with every scale. Indices with scale-numbers below 11 can not solve any star fields because they contain too few quads. This arises from the fact that all index files are built with a star list that contains only sources with a maximum apparent magnitude of 8. This limits the number of quads that can be created at small scales. For all other indices, the precision of the calibration decreases with increasing scale-number. The median of pointing deviations is nearly constant at scale-numbers from 11 to 13. Since the upper limit of the 99% containment interval is lowest for scale-number 12 (except scale-number 11 with quad-dimension 3 where some star fields can not be calibrated) this scale number is supposed to be most suitable. An index file with four-dimensional quads with scales between 120 and 170 arcminutes is therefore used for all previous and further pointing reconstructions.

6.4 Simulating Different Magnitudes

For the astronomical calibration of images, it is crucial how many stars are visible in an image. Apart from obstructing objects in the field-of-view, the number of visible stars depends on the minimal brightness that a star has to have in order to be visible in the image. The most important influencing factors on this minimal brightness are exposure time, aperture and noise of the chip, but also the night sky background. To

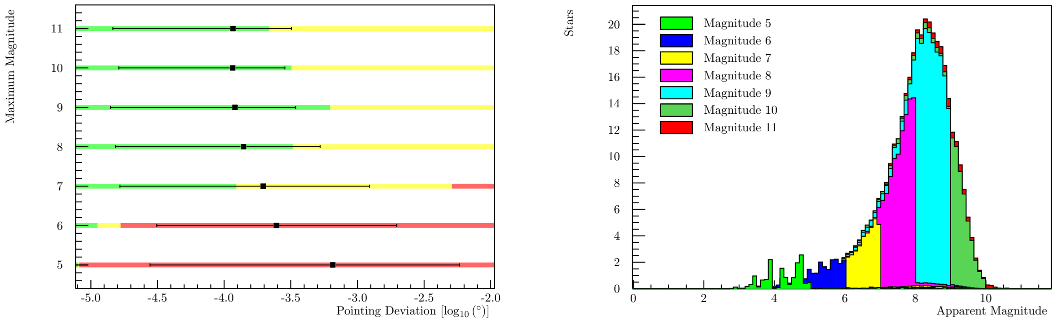

Figure 6.5: Left: Medians and 99% containment intervals of distributions of reconstruction deviations for different maximum magnitudes. Right: Average magnitude distributions of matched stars for star fields with different maximum magnitudes.

study the precision of the calibration as a function of the number of visible stars, different sets of star fields are simulated with maximum apparent magnitudes from 1 to 11. For these reconstructions, a special index file is created that contains stars with magnitudes up to 11. It comprises 4-dimensional quads with a scale number of 12. Figure 6.5 shows the characteristics of the distributions of the resulting pointing deviations and the corresponding average magnitude distributions of stars that can be matched in the calibration.
The simulations of star fields with maximum magnitudes of less than 5 are not included in the plot because none of these can be calibrated due to the small number of stars. Up to magnitude 7 more and more star fields can be calibrated. Beginning at magnitude 8, all reconstructions succeed. The precision of the calibrations increase with an increasing number of stars in the simulations. This is most likely due to better WCS fits which become possible with more available stars. In contrast to that, the number of “bad” reconstructions is increased in comparison to reconstructions with index files that only comprise stars with magnitudes up to 9. This may be because if an index file contains too many stars, some stars in an image are identified with wrong stars, that are close to the true positions. The magnitude distributions also show that the number of matched stars, and therefore the number of used stars in the calibration, does not increase significantly with the simulation of stars with magnitudes greater than 10.

6.5 Exposure and Aperture

While all previously discussed pointing reconstructions emanate from exactly known star positions in an image, the following paragraphs deal with astronomical calibration of images that are simulated pixel by pixel. As mentioned in Section 5.4, the simulation approximates the image of a star as a two-dimensional Gaussian distribution. The amplitude of this distribution depends on the luminosity of the star, the size of the aperture,

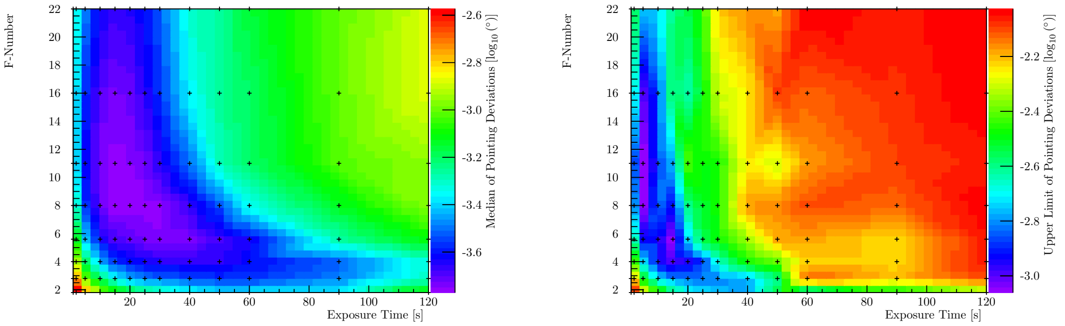

Figure 6.6: Left: Medians of distributions of reconstruction deviations for different aperture sizes and exposure times. Black plus signs mark simulated configurations. The colored histogram is an interpolation with Delaunay triangles. Right: The same plot for upper 99% limits of reconstruction deviations.

and the exposure time. The width of the distribution depends only on the aperture. Due to the azimuthal mount of the telescope, an increased exposure time also increases the rotation of the field-of-view. This results in star images, that are segments of circles around the center of the image. Each point on such a circle corresponds to the star position at a certain point in time during the exposure. To achieve a precise calibration, the source extraction algorithm must output all star positions at the same point in time. Less rotation of the field-of-view will reduce errors that arise from this problem. This means that the exposure time should be chosen as short as possible. On the other hand, short exposure times also come along with darker star images, so that some fainter stars can not be used for the calibration at all. This can be compensated with the use of wider apertures, which allow for the collection of more light in the same time. The downside of this are increasing widths of star images, which make it more difficult to identify the center of each star.

Therefore an optimal configuration of exposure time and aperture has to be found. This is done by simulating and reconstructing sets of images with different f-numbers and exposure times. For each configuration, as many images as possible are simulated over a time of 24 h. Figure 6.6 shows the medians and upper 99%-limits of the resulting pointing deviations. The resulting values for the plotted data are listed in Table D.1 and D.2. The smallest values for the median are in an area around f-numbers 8 and 11 and between exposure times of 10 and 25 seconds. The highest precision of the most inaccurate calibrations is found at two points. One minimum is at an exposure time of 5 s and at f-numbers 8 and 11. Another local minimum is at an exposure time of 20 s and f-numbers 4 and 5.6. These promising ranges should be examined further when the configuration for real pointing images is determined.

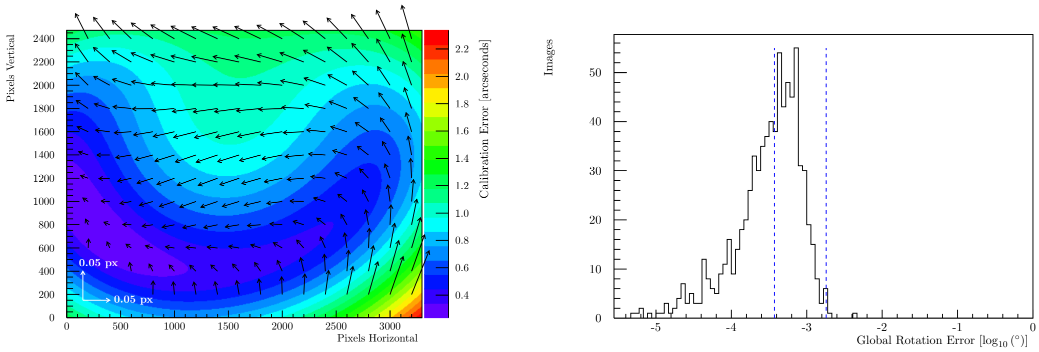

Figure 6.7: Left: Pointing errors for all pixels in a simulated, calibrated image with an exposure time of 5 s and an f-number of 8. Arrows indicate differences between reconstructed and expected positions of a certain location in the sky. They are scaled with a factor of 500 (see bottom left corner). Right: Distribution of global rotations in the pointing errors of simulated images with this configuration. The median and the upper 99%-limit are indicated with blue lines.

6.6 Calibration Errors within a Pointing Image

All previous discussions only include differences between the reconstructed position of the image center and its original position. But it is also important to know how the calibration maps other points in an image to positions in the sky. To illustrate this, an exemplary image is simulated with an exposure time of 5 s and an f-number of 8. At the usual start time, the camera points to (Az, Alt) = (70°, 70°). This image is calibrated and the corresponding position in the sky is calculated for each pixel. This is compared to the expected sky-position of each pixel. The angular distance between the reconstructed and expected point on the sphere is referred to as the pointing error of a given pixel. The pointing errors in the exemplary image are plotted in Figure 6.7. The plot also includes arrows that point exactly to the position in the image, where the location in the sky that the point of their base is calibrated to, is expected to be mapped to the image. The arrows are scaled for better visibility.

The pointing errors are relatively small in the whole image ($< 2.4''$). The smallest errors are not necessarily in the center of an image. Expressed in pixels, all pointing errors in the image are smaller than 0.1 pixel. These errors are likely to originate from numerical uncertainties in the fit of the WCS at the end of the calibration algorithm. Improvements to this polynomial fit may increase the precision of the pointing calibration. Because of time constraints, this is not investigated further in this thesis.

One important portion of the pointing errors of a calibrated image is a global rotation around the center. This is derived for a given image by calculating the rotation

$$\operatorname{rot} F(x, y) = \frac{F_y(x + \Delta x, y) - F_y(x, y)}{\Delta x} - \frac{F_x(x, y + \Delta y) - F_x(x, y)}{\Delta y} \tag{6.1}$$

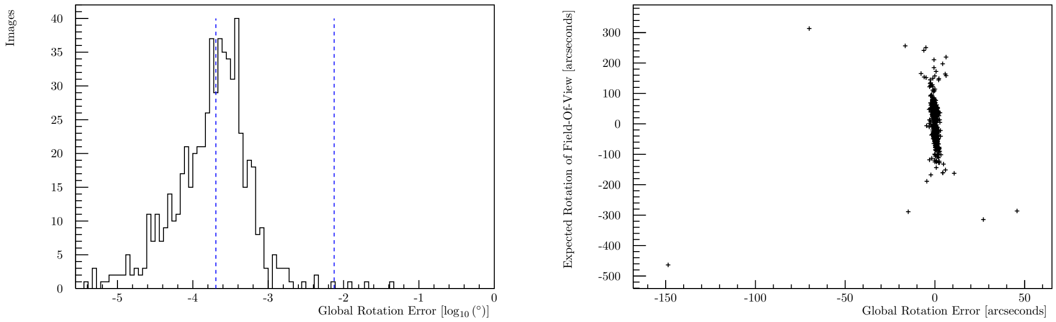

Figure 6.8: Left: Distribution of global rotations in the pointing errors of simulated images with an exposure time of 30 s and an f-number of 8. Right: Correlation between rotations and expected rotation of the field-of-view.

at each pixel (x, y), where $F_x(x, y)$ is the horizontal and $F_y(x, y)$ the vertical component of the pointing error at that pixel. For Δx and Δy a value of 10 is chosen. The mean rotation $\langle \mathrm{rot}\, F(x, y)\rangle$ for all pixels in the given image is then calculated and the angle ϕ of the global rotation is derived:

$$\phi = \arcsin\left(\langle \mathrm{rot}\, F(x, y)\rangle / 2\right)/\pi \cdot 180 \cdot 3600'' \tag{6.2}$$

The distribution of this rotation angle for a set of simulated images with the above-named configuration is plotted in Figure 6.7. The upper 99%-limit is $6.6''$, the median of the distribution is $1.3''$. In Figure 6.8, the same distribution is plotted for a set of simulated images with exposure times of 30 s. For this longer exposure time, there are more images with rotation errors greater than $10''$. Here, the upper 99%-limit is $26.7''$. A graph, that illustrates the correlation between the rotation error and the expected rotation of the field-of-view during the exposure (calculated with 3.8), is also plotted in Figure 6.8. This shows, that images with great rotation errors are also images with strong rotations of the field-of-view.

To study the rotation errors systematically, sets of images with different exposure times and f-numbers are simulated and calibrated with the same configurations as in 6.5. Figure 6.9 shows the medians and upper 99%-limits of the resulting distributions. The numerical values are listed in Table E.1 and E.2. As expected, the rotation errors tend to be smaller for shorter exposure times. The smallest values for both the median and the upper 99%-limit result for an f-number of 11. The best precisions are achieved at exposure times of $5 - 30$ s, while the median is smaller at longer exposure times, whereas the upper 99%-limit is smaller at shorter exposure times.

The presented results show, that a possible improvement to the real-world calibration could be a reduction of the exposure time at pointing positions, where strong rotations of the field-of-view are expected. Images with smaller rotations can be taken with longer exposure times.

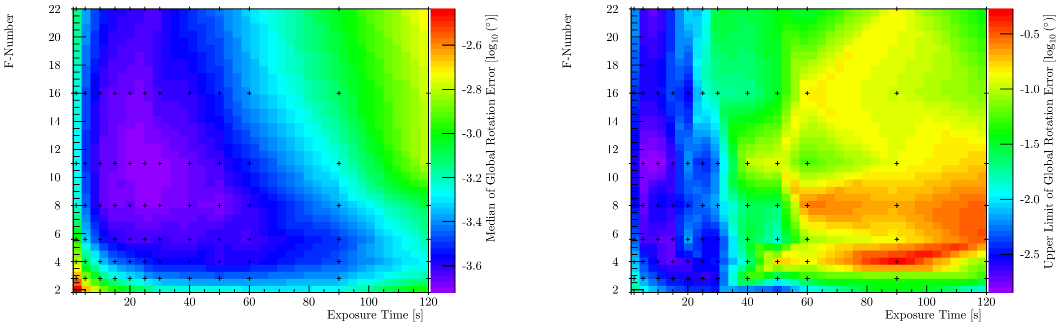

Figure 6.9: Left: Medians of distributions of rotation errors for different aperture sizes and exposure times. Right: The same plot for upper 99% limits of rotation errors.

6.7 Summary

In this chapter, it has been shown that pointing images simulated with `libCCDCamera` can be analyzed sensibly with `libPointingMST`. If all star positions in an image are known precisely, the celestial coordinates of the image center can be determined to a precision of better than $2''$ for a simulated pointing camera as described in Chapter 4. There is also a second class of reconstructions, that only show a precision of the order $0.1°$. The origin of this class is not yet understood but the images in question can be rejected either by increasing the log odds limit or by analyzing the ratio (matched stars/stars in field of view). If an obstructing square Cherenkov camera with an edge length of 3 m is added to the simulation, the precision drops to $3.6''$. It has been shown, that index files with 4-dimensional quads with a scale-number of 12 are suitable for the given image scale. It became clear that increasing the maximum magnitude of simulated stars in an image does only improve the precision of the calibration up to a value of 9. It has also been studied, which exposure times and which f-numbers suit best for taking pointing images. The best result have been obtained for exposure times of 5 s - 20 s and f-numbers between 4 and 11. It has been proven, that the rotation of an image in the chip-plane can be determined to a precision of better than $6.6''$ for short exposure times and that this precision relates to the rotation of the field-of-view during an exposure. For longer exposure times of 30 s, this precision drops to about $0.5'$. However, even this larger uncertainty should not influence the telescope pointing significantly because it does not correlate with the actual alignment of the instrument if the optical axes of CCD-camera and telescope are parallel. It only corresponds to the uncertainty of the rotation of the Cherenkov camera and a rotation of $0.5'$ results in an offset of < 1 mm at the edge of a typical Cherenkov camera, which has a pixel size of several centimeters.

7 Real Images of the Sky

In this last chapter, a test setup at the Dr. Karl Remeis-Sternwarte in Bamberg is described. With this installation, images of the sky are captured with the complete camera and housing setup discussed in Chapter 4. Therefore, the structure is attached to a mount for a telescope in order to being able to align the camera to defined positions in the sky. The obtained images are then analyzed with `libPointingMST` and the results are compared to those of the previously discussed simulations.

7.1 Test Setup in Bamberg

Due to its large mass, it is not possible to attach the camera together with the housing to a portable telescope mount on a tripod. So the mount in the western dome of the Dr. Karl Remeis-Sternwarte in Bamberg is considered to be a feasible solution because this telescope mount is vacant due to telescope maintenance for several weeks during the compilation of this master's thesis. It is a German equatorial mount, that allows for automatic tracking and observations of positions in the sky, either defined by equatorial or by azimuthal coordinates.

The camera is focussed to a distance of 32 m using a checkerboard pattern in advance to these tests.

The housing is attached to the mount via a special dovetail rail fixed to its all-aluminum feet. The tracking system is roughly calibrated with the known position of Venus, whose image is aligned with the center of the CCD-chip. This calibration is done to a precision of about 0.4°. A captured image with Venus at its center is shown in Figure 7.1. This image also shows that parts of the dome sometimes cover certain parts of an image because the dome can only be opened up to about 20°.

7.2 Exemplary Comparison with the Simulation

In order to check if simulations with `libCCDCamera` are consistent with real images, an exemplary image is captured and simulated with the same parameters. The camera points to (Az, Alt) = (135°, 45°), the exposure time is 10 s and the f-number is 5.6. The CCD-Chip is cooled to a temperature of -5 °C. Figure 7.2 shows three times the same part of the sky, once photographed with active tracking, once with a fixed alignment of the camera, and once as a simulation. For better visibility of the individual stars, a section close to the edge of the images is shown. The simulated image is also rotated to fit the orientation of the camera on the equatorial mount.

Figure 7.1: An image used for calibrating the tracking system of the telescope mount. Venus appears as a bright spot in the center. In the upper left corner, a part of the dome obstructs the view to the sky.

The images show great conformity on the first view. There is a slight difference in the scale of simulated and real images: The simulated image has to be scaled up ~ 1% to be congruent with the real images. This is likely due to the adapter between the CCD-camera and the lens, which changes the distance between the chip and the lens and scales up the image. The stars in the image with deactivated tracking appear as distinct lines, whereas the expected rotation of the field-of-view in the simulated image is not as distinctive. The real images also show so-called "hot rows", imaging errors that arise from the sequential read-out technique of the CCD-chip. Another difference between the simulation and the imaged sky can be seen close to the right edge in the middle of the image. The star ϵ Del is not included in the simulation. Such a discrepancy is also observable in another part of the same image (not visible in the figure): Altair is also missing in the simulation. This may be a hint, that the star catalogue of the H.E.S.S. software is incomplete. The second image also comprises the visible track of an artificial satellite.

Another difference between the simulation and the real images can be seen in their magnitude distributions. Figure 7.3 shows the apparent magnitudes of all stars that are recognized by `Astrometry.net`. For brighter stars, where discrepancies can be explained by the differing field-of-view, the distributions are quite similar. From a magnitude of ~ 7.5, the number of stars drops very quickly for the simulated image although the simulation is configured such that it adds stars up to a magnitude of 10 to the image. However,

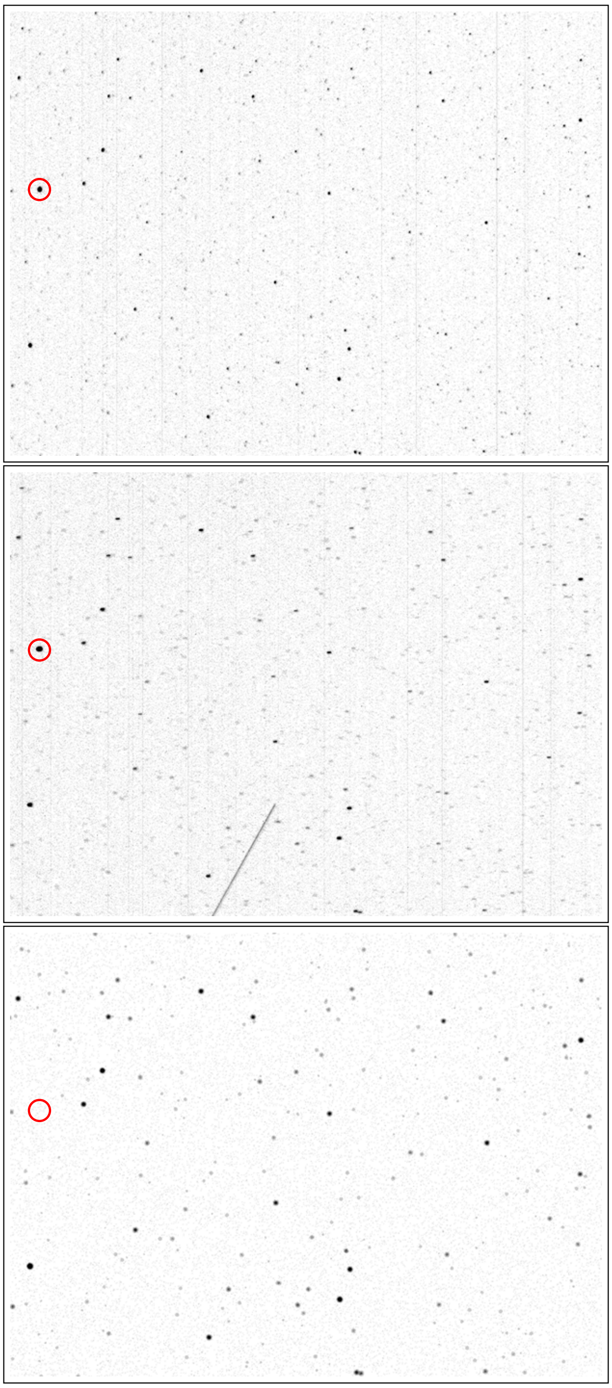

Figure 7.2: Three image-sections of the same part of the sky. The first is a photo taken with activated equatorial tracking. The second is a photo taken with a fixed camera. The third is a simulation. Images are brightened and inverted for better visibility. The position of the star ϵ Del is marked with a red circle.

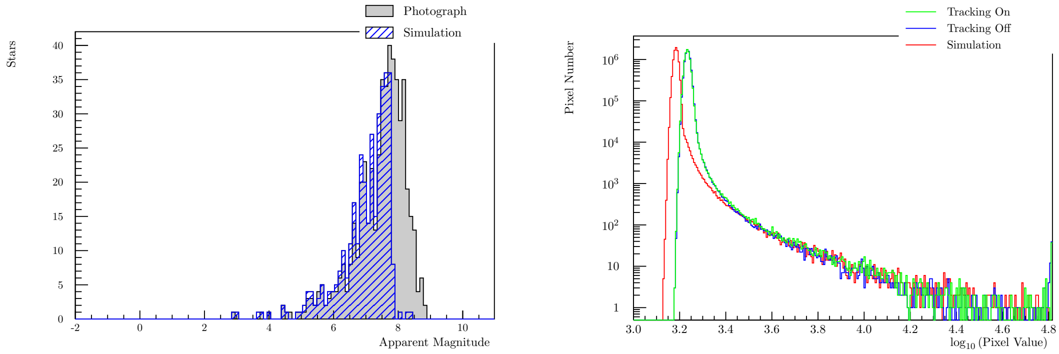

Figure 7.3: Left: Magnitudes of matched stars in the exemplary images from 7.2 for the simulation (blue) and the photograph with activated tracking (gray). Right: Image histograms for the three images.

the photography comprises more stars up to a magnitude of ~ 9. This lack of fainter stars in the simulated image is likely to result from nonlinear light collection properties of the real-world instrument, which are currently not included in the simulation. In total, 510 of 858 extracted sources in the photograph can be matched to known stars. In the simulated image, 378 sources are extracted, of which 354 can be matched.

Some difference can also be seen in the histograms of the images, which are plotted in Figure 7.3. The light of the night sky background shifts the noise-peak to higher intensities in the real images in comparison to the simulation. This may be superimposed by the light of the fainter stars that are not visible in the simulated image. At higher intensities, the discrepancies between simulation and real image completely vanish. There is also no significant difference between the image that was captured with activated tracking and the one with a fixed camera.

7.3 Pointing Scan of the Sky

In order to test the hardware and the pointing reconstruction technique presented in this thesis, a scan of the hemisphere above the telescope mounting is done, similar to a pointing-run of an IACT. Therefore, images at 24 grid positions are captured. The azimuth is scanned from 0° to 315° in steps of 45°. Altitudes of 20°, 45°, and 70° are used. For each position that is selected via the electronic control of the telescope mount, two images are taken: one image with activated tracking, and one with a fixed alignment of the camera. These two imaging modes are deployed because they both approximate the case of a camera on an azimuthal mount, which features a rotation of the field of view. All images are taken with an exposure time of 10 s and an f-number of 5.6. The scan is done on July 10, 2015.

The resulting images are then calibrated with `libPointingMST`, using an index file with stars with magnitudes up to 11 and 4-dimensional quads with scale number 12. In the

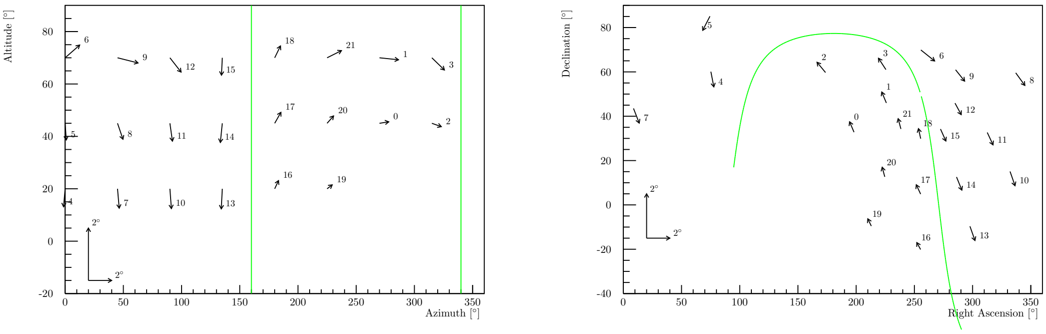

Figure 7.4: Differences between expected coordinates and reconstructed coordinates represented by arrows for an azimuthal grid. All arrows are scaled by a factor of 10 (see bottom left). The arrows are numbered in the chronological order of the corresponding images. Left: Azimuthal coordinates. Green lines at azimuths 160° and 340° mark the positions where the telescope mount rotates the camera 180° around both axes. Right: Equatorial coordinates. The right ascension of all arrows is corrected as if all exposures were done at the same point in time. Green lines are equivalent to those in the left plot.

first discussion, only the images with active tracking are analyzed. The calibration of 2 of these 24 images fails because the night sky is partly covered by clouds in these images. For each successful reconstruction, the calibrated RA/Dec coordinate of the image center is determined. This is compared to the expected RA/Dec coordinate, which can be calculated with the selected position of the mount, the location of the observatory and the time of the exposure. The reconstructed Alt/Az coordinate is also calculated and compared to the selected position. The resulting differences for both coordinate systems are plotted in Figure 7.4.

All deviations from the expected directions are in the order of 0.5°, which is also about the precision of the initial calibration of the tracking system. But the observed deviations can not be explained solely by an initial misalignment, which would lead to a constant offset in equatorial coordinates. A composition of a global offset and a mechanic bending of the support feet of the camera housing is more likely. Due to the large mass of the housing and the insufficient rigidity of the all-aluminum rails, deformations by gravity are expectable. Such deformations are expected to depend on the orientation of the housing relative to gravity.

At the azimuth angles 160° and 340° discontinuities in the directions of the pointing deviations are observed. This is likely due to a peculiarity of the telescope mount: At these positions, the counterweight of the mount is above the attachment for the telescope and the latter gets relatively close to the pillar that holds the mount. In order to avoid a collision of the telescope with this pillar, the mount rotates the camera housing 180° around its both axes. This does not change the observation direction but rotates the field-of-view and inverts the direction of gravity relative to the housing.

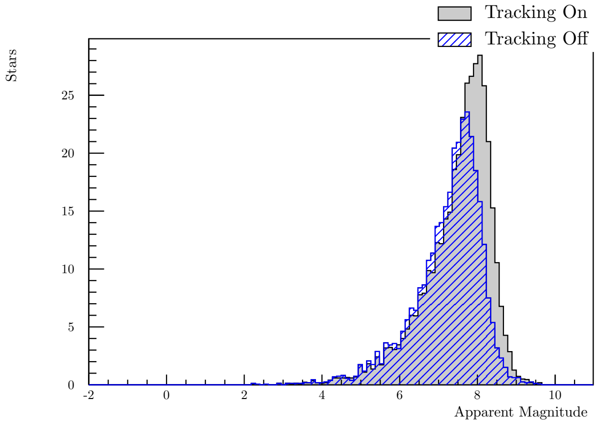

Figure 7.5: Average magnitudes of matched stars in images from the scan of the sky with activated tracking (gray) and without tracking (blue).

The images with deactivated tracking are also analyzed with `libPointingMST`. Seven of these 24 images can not be calibrated with the previously described index file. These are mostly images with small altitude, where obstacles like trees or clouds cover the sky. This suggests that the calibration is less robust for images with blurred stars. The average distribution of magnitudes of recognized stars shows, that there are fewer matched stars and especially fewer darker sources in these images than in images with activated tracking (see Figure 7.5). Fainter stars are not visible as clearly in an image where the stars are moving because their light can not be collected in a few pixels but is spread over a larger area on the chip. The faintest stars that can be matched have magnitudes of ~ 9.6 for both tracking configurations.

7.4 Summary

In this chapter, a test setup at an observatory has been described. A captured image has been compared exemplarily to a simulated image and the differences between simulation and real images have been discussed. It became clear that the field-of-view and the efficiency of the light collection are not accurately reproduced in the simulation. A grid scan of the sky has shown that it is possible to reconstruct the direction of pointing images with the means that have been introduced in the previous chapters and that the hardware whose development that has been described in Chapter 4 is applicable for taking such images. Due to the insufficient rigidity of the all-aluminum support feet of the housing, it can not be determined whether the attachment of the CCD-camera to the housing is rigid enough.

8 Summary and Outlook

In this thesis, a possible Single-CCD pointing solution for the medium-sized telescopes of CTA has been presented. This solution comprises an astronomical CCD-camera with a wide angle objective, that is integrated in a rigid housing which can be attached to a telescope. The first prototype of this housing was similar to the one that is currently in use at the H.E.S.S. gamma-ray observatory. The housing has been developed further, so that the electronics and optics of the camera are shielded from environmental impact but that they also stay below their maximum operating temperature. This has been achieved by improving the thermal conduction from the CCD-camera to the surrounding air with heat conduction structures and passive heat sinks. It has been shown, that the temperature inside the improved housing stays below 40 °C at an environmental temperature of 25 °C during a simulated operation.

Further improvements are still necessary to reduce the mass and costs of the housing. The problem of water and dust proof cable feedthroughs has still to be solved.

A software library called `libCCDCamera` has been introduced in this thesis. This library can be used to simulate images that could be captured by the CCD-camera if it was mounted to a telescope. Another library, namely `libPointingMST`, has been developed, which can calibrate such pointing images and makes transformations from pixel coordinates to celestial coordinates and vice versa possible. This library uses the algorithms of the open source software `Astrometry.net`.

The astronomical calibration has been tested with $\sim 2{,}000{,}000$ simulated images and the dependencies of its precision of different parameters have been investigated. It has been proven, that the pointing of a CCD-camera with a lens with a focal length of 50 mm mounted to an IACT can be reconstructed with residual errors of less than $4''$ even though about 36% of the field of view is obstructed by a Cherenkov camera.

In the last chapter of the thesis, the measurements on a real-world setup with the telescope mount of an observatory has been described. With this setup, images of the sky could be taken at defined pointing positions. These images have been used to verify the simulations with `libCCDCamera`. One significant difference between simulations and real images is an underestimation of light collection at low fluxes. This leads to fewer visible stars with magnitudes over 8 in simulated images than in real images.

A scan in an azimuthal grid of the hemisphere above the telescope mount has proven that the deployed hardware and software work as expected. The calibration of the captured images has shown deviations to the grid positions in the order of the precision of the initial alignment of the camera on the mount. The results also show that the support feet of the housing are subject to mechanical deformations under gravity.

The next steps towards a solution for measuring the pointing of the medium-sized telescopes of CTA include some minor optimizations to the telescope housing and test series on a telescope prototype or on one of the first constructed instruments. There, pointing-runs could be tested on an azimuthal mount. A reference measurement of the pointing could also be used to verify the astronomical calibration. Such a reference measurement could be implemented for example with an accelerometer and a gyroscope, which are build in most smartphones.

For more detailed studies with simulated images, `libCCDCamera` has to be developed further, so that the observed nonlinearities in the efficiency are emulated more exactly.

There are also a lot of improvements necessary for `libPointingMST` to become a library that can be used in production software of CTA. Besides some memory management issues, there are several functions that are yet to be implemented. This includes for example the procession of the Pointing-LEDs or the creation of a pointing model.

The imaging of the Pointing-LEDs and the resulting systematic errors of potential reconstruction deviations have not yet been investigated. It is also unclear, how strong the impact of distortions by the lens is on the pointing calibration. The simulation library already supports a radial symmetric distortion function but this feature has not been used yet. Another interesting setup could be a camera that is mounted in the canter of the dish but is aligned to the side of the Cherenkov camera, with an angular offset to the optical axis of the telescope, similar to the Precision Pointing-Concept. The influence of optical distortions on this concept could be the subject of further studies. Other effects like atmospheric refractions or the different light spectra of stars and their influence on the precision of the pointing reconstruction could also be investigated further.

Appendices

A Product Datasheet CCD-Camera

Aspen CG8050 | High Performance Cooled CCD Camera System

ANDOR an Oxford Instruments company

System Features[*1]

- **High Resolution Sensor**
  8.2 Megapixel sensor with 5.5 μm pixels delivers an exceptionally large field of view with high resolution.
- **Programmable TE cooling down to 60°C below ambient**
  Ideal for detection of weak chemiluminescence or astronomy images, enabling long exposure acquisitions with optimized signal to noise ratio.
- **Ethernet interface with built-in web server**
  Remote access and control over the Internet, via standard web browser.
- **USB 2.0 interface**
  Direct 'Plug and Play' simplicity of USB 2.0.
- **16-Bit digitization**
  High photometric accuracy.
- **High longevity shutter**
  Shutter during readout and take dark reference frames - 35 mm.
  Specified for >5 million cycles.
- **Programmable I/O port**
  Synchronization with intricate experimental set-ups.
- **Remote Triggering**
  LVTTL input allows exposure to start within 25 microseconds of the rising edge of the trigger.
- **Focusing mode**
  Faster readout option, ideal for focus optimisation.
- **Precision locking filter wheels optional**
  Choose from a range of Apogee family filter wheels with up to 17 positions.

Apogee Aspen CG8050: Compact, 8.2 Megapixel CCD

Ideally suited to challenging astronomy and physical science imaging applications, the Apogee Aspen family offers a range of popular full frame and interline CCD sensors, within a camera platform that is designed to push performance. Deep thermoelectric cooling ensures optimal sensitivity for long exposure applications. The simple convenience of a USB 2.0 interface is accompanied by an Ethernet network interface with a built-in web server. The Apogee Aspen also utilizes a new extremely high reliability shutter, specified for > 5 million shutter cycles.

The Aspen CG8050 has a 8.2 megapixel format interline transfer CCD sensor with low noise and high quantum efficiency and small 5.5 μm pixels. Cooling down to 60°C below ambient results in a low dark current contribution. These features combine to make the CG8050 ideal for microscopy applications requiring both high resolution and large field of view.

Specifications Summary[*1]

Array Size (pixels)	3296 x 2472 (8.2 Megapixel)
Pixel Size	5.5 x 5.5 μm
Sensor Size	18.1 x 13.6 mm (246.5 mm^2) 22.7 mm diagonal
Pixel Well Depth (typical)	18,000 e^-
Dark Current[*2]	0.0061 e^-/pixel/sec
Read Noise[*3]	10.8 e^- (RMS @ 0.91 Mhz)
Maximum Dynamic Range	64.4dB (1667:1)
Quantum Efficiency	50% maximum @500 nm 32% @400 nm

1

Figure A.1: Product datasheet Apogee Aspen CG8050 – page 1

Aspen CG8050

High Performance Cooled CCD Camera System

ANDOR
an Oxford Instruments company

SPECIFICATIONS

Technical Specifications*1

Sensor Type	KAI-08050 (ON Semiconductor)
Active pixels	3296 x 2472 W x H (8.2 Megapixel)
Sensor Size	18.1 x 13.6 mm (246.5 mm^2) 22.7 mm diagonal
Pixel Size	5.5 x 5.5 µm
Pixel Well Depth	18,000 e$^-$
Read Noise *3	10.8 e$^-$ (RMS @ 0.91 MHz)
Pixel Binning	1 x 1 to 8 x 2472 on chip
Quantum Efficiency*4	50% maximum @500 nm 32 % @400 nm
Cooling	Maximum cooling up to 60°C below ambient temperature ; -35°C at 25°C ambient Thermoelectric cooler with forced air.
Temperature Stability	+/- 0.1°C
Dark Current*3	0.0061 e-/pixel/sec
Blemish Specification	Grade S as per sensor manufacturer definition
Anti-blooming factor	>300x
Maximum Dynamic Range	64.4 dB (1667:1)
Linearity	Better than 99%
Frame Rate (fps)*5	0.11 Full frame (@0.91 MHz) 0.87 Full frame (@7.31 MHz, focusing mode)
Frame Sizes	Full frame, sub-frame
Digital Resolution	16-bit
Camera Window	UV-grade fused silica

General Specifications

Interface Options	USB 2.0 Ethernet: Network interface with built-in web server, up to 2 MHz throughput
Remote Triggering	LVTTL trigger input, expose strobe output
Peripheral communications	8 pin mini-DIN I/O connector
Image Sequencing	1 to 65535 image sequences under software control
Exposure Time	100 milliseconds to 183 minutes (2.56 microsecond increments)
Operating System Support	Windows, Linux

2

Figure A.2: Product datasheet Apogee Aspen CG8050 – page 2

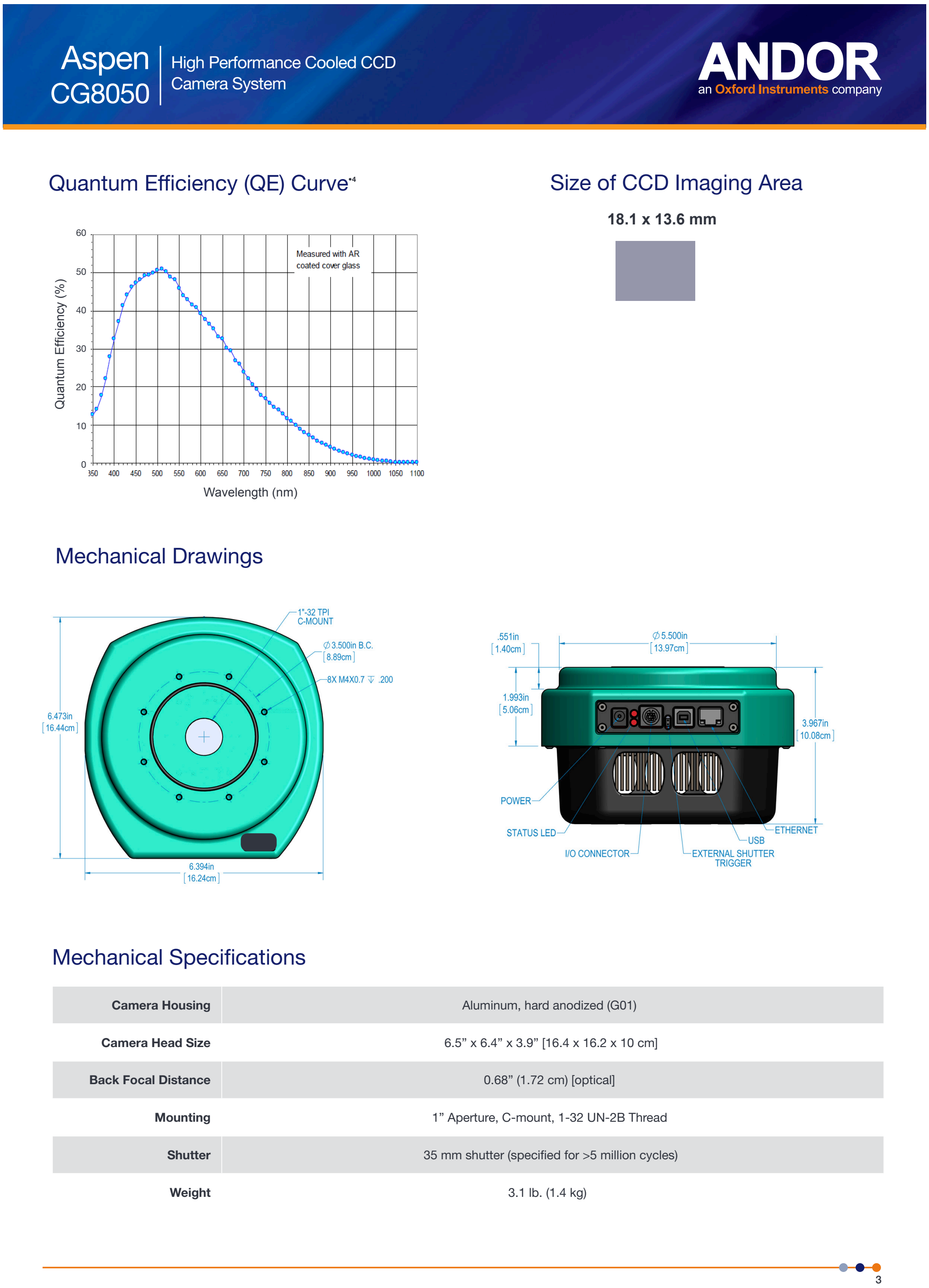

Aspen
CG8050

High Performance Cooled CCD
Camera System

ANDOR
an Oxford Instruments company

Quantum Efficiency (QE) Curve*4

Size of CCD Imaging Area

18.1 x 13.6 mm

Mechanical Drawings

Mechanical Specifications

Camera Housing	Aluminum, hard anodized (G01)
Camera Head Size	6.5” x 6.4” x 3.9” [16.4 x 16.2 x 10 cm]
Back Focal Distance	0.68” (1.72 cm) [optical]
Mounting	1” Aperture, C-mount, 1-32 UN-2B Thread
Shutter	35 mm shutter (specified for >5 million cycles)
Weight	3.1 lb. (1.4 kg)

3

Figure A.3: Product datasheet Apogee Aspen CG8050 – page 3

B Product Datasheet CCD-Sensor

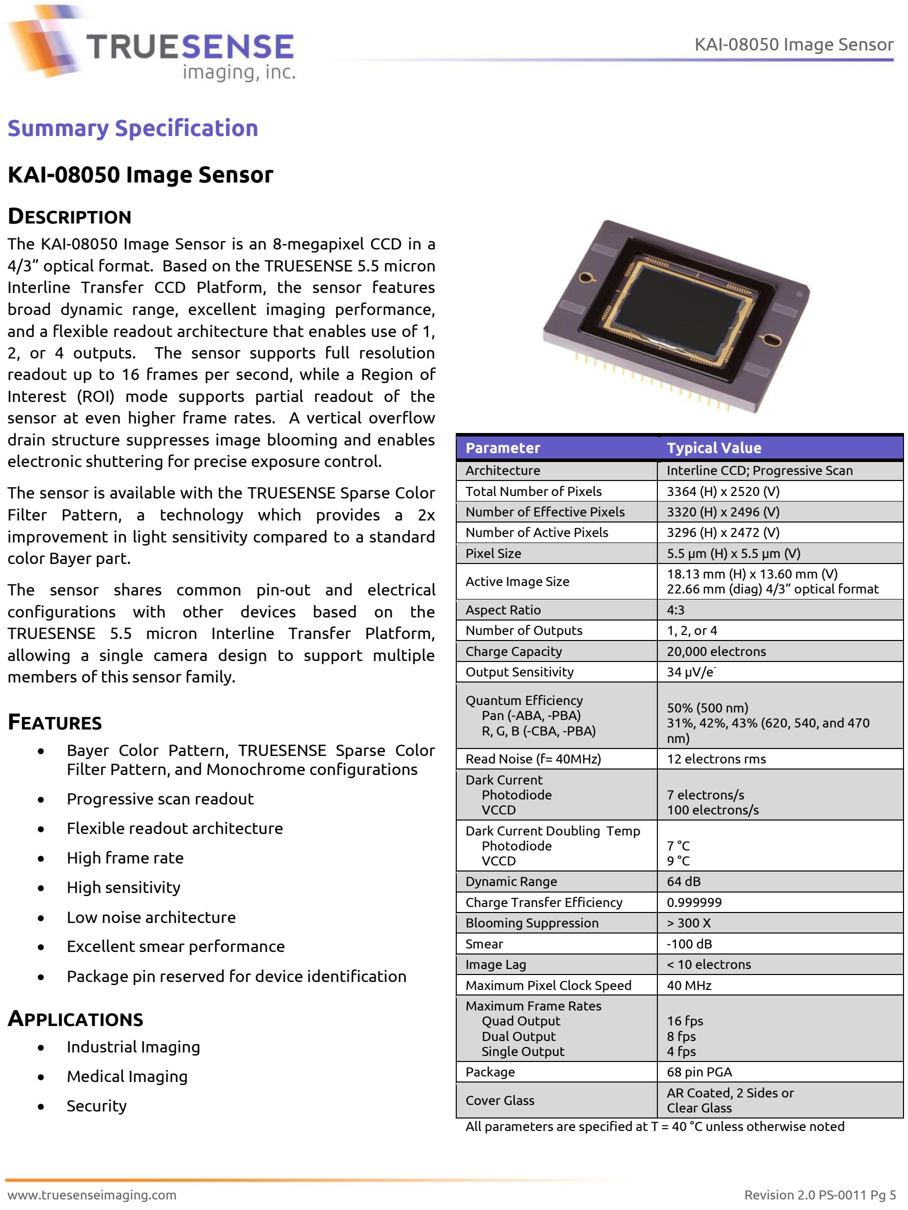

TRUESENSE imaging, inc.

KAI-08050 Image Sensor

Summary Specification

KAI-08050 Image Sensor

DESCRIPTION

The KAI-08050 Image Sensor is an 8-megapixel CCD in a 4/3” optical format. Based on the TRUESENSE 5.5 micron Interline Transfer CCD Platform, the sensor features broad dynamic range, excellent imaging performance, and a flexible readout architecture that enables use of 1, 2, or 4 outputs. The sensor supports full resolution readout up to 16 frames per second, while a Region of Interest (ROI) mode supports partial readout of the sensor at even higher frame rates. A vertical overflow drain structure suppresses image blooming and enables electronic shuttering for precise exposure control.

The sensor is available with the TRUESENSE Sparse Color Filter Pattern, a technology which provides a 2x improvement in light sensitivity compared to a standard color Bayer part.

The sensor shares common pin-out and electrical configurations with other devices based on the TRUESENSE 5.5 micron Interline Transfer Platform, allowing a single camera design to support multiple members of this sensor family.

FEATURES

- Bayer Color Pattern, TRUESENSE Sparse Color Filter Pattern, and Monochrome configurations
- Progressive scan readout
- Flexible readout architecture
- High frame rate
- High sensitivity
- Low noise architecture
- Excellent smear performance
- Package pin reserved for device identification

APPLICATIONS

- Industrial Imaging
- Medical Imaging
- Security

Parameter	Typical Value
Architecture	Interline CCD; Progressive Scan
Total Number of Pixels	3364 (H) x 2520 (V)
Number of Effective Pixels	3320 (H) x 2496 (V)
Number of Active Pixels	3296 (H) x 2472 (V)
Pixel Size	5.5 μm (H) x 5.5 μm (V)
Active Image Size	18.13 mm (H) x 13.60 mm (V) 22.66 mm (diag) 4/3” optical format
Aspect Ratio	4:3
Number of Outputs	1, 2, or 4
Charge Capacity	20,000 electrons
Output Sensitivity	34 μV/e$^-$
Quantum Efficiency Pan (-ABA, -PBA) R, G, B (-CBA, -PBA)	50% (500 nm) 31%, 42%, 43% (620, 540, and 470 nm)
Read Noise (f= 40MHz)	12 electrons rms
Dark Current Photodiode VCCD	7 electrons/s 100 electrons/s
Dark Current Doubling Temp Photodiode VCCD	7 °C 9 °C
Dynamic Range	64 dB
Charge Transfer Efficiency	0.999999
Blooming Suppression	> 300 X
Smear	-100 dB
Image Lag	< 10 electrons
Maximum Pixel Clock Speed	40 MHz
Maximum Frame Rates Quad Output Dual Output Single Output	16 fps 8 fps 4 fps
Package	68 pin PGA
Cover Glass	AR Coated, 2 Sides or Clear Glass

All parameters are specified at T = 40 °C unless otherwise noted

www.truesenseimaging.com

Revision 2.0 PS-0011 Pg 5

Figure B.1: Product datasheet Kodak KAI-08050

C UML Class Diagram of Simulation

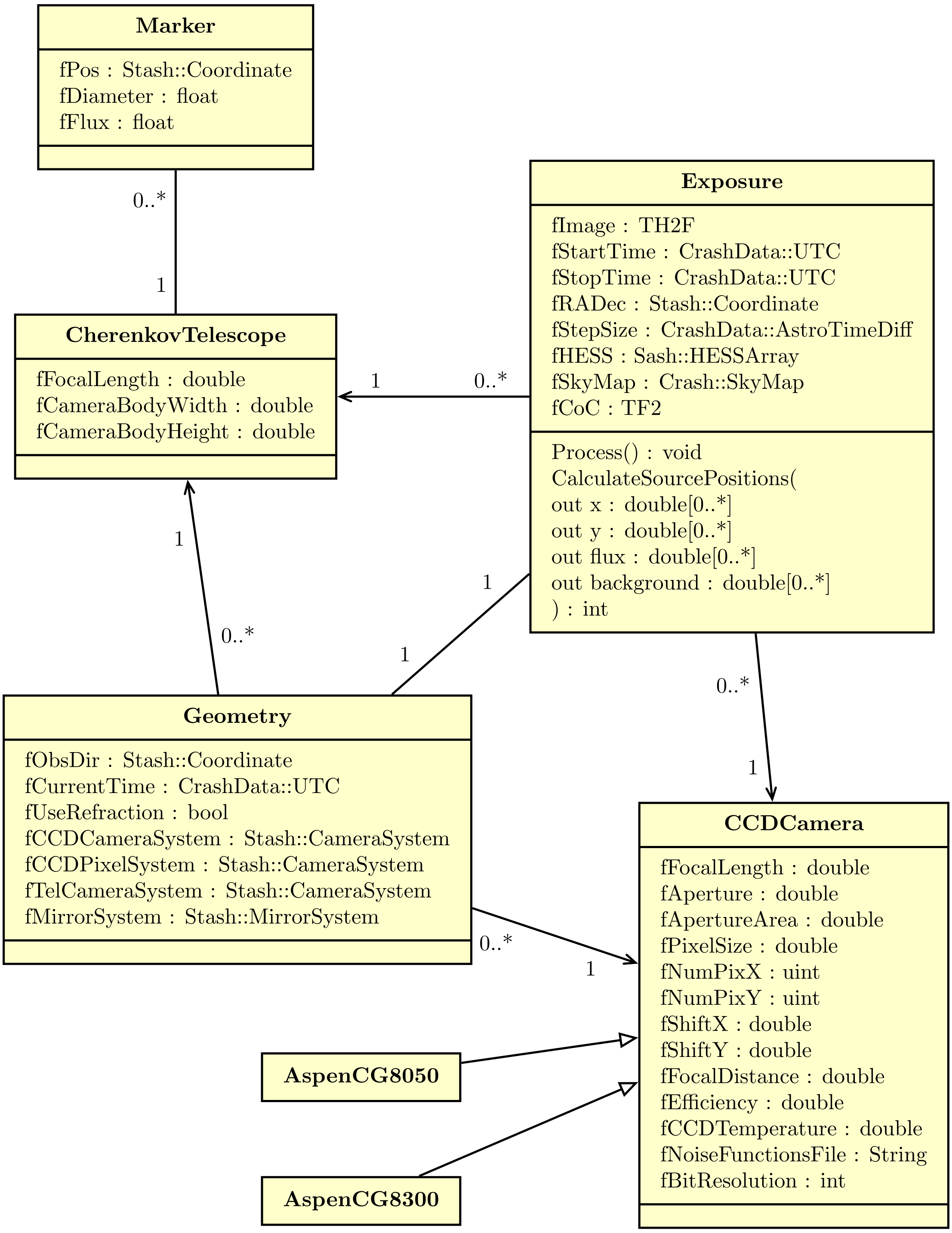

Figure C.1: UML class diagram of `libCCDCamera`. Only the most important parameters and methods are shown.

D Exposure and Aperture Results

Table D.1: Medians of pointing deviations.

F-Number	1.8	2.8	4	5.6	8	11	16	22
Exposure [s]								
1	-2.32	-2.53	-2.71	-2.9	-3.06	-3.17	-3.23	-3.08
2	-2.47	-2.71	-2.90	-3.08	-3.27	-3.37	-3.36	-3.31
5	-2.73	-2.97	-3.18	-3.40	-3.57	-3.61	-3.57	-3.48
10	-2.93	-3.20	-3.43	-3.62	-3.72	-3.74	-3.70	-3.62
15	-3.24	-3.50	-3.65	-3.75	-3.76	-3.66	-3.57	-3.52
20	-3.04	-3.35	-3.56	-3.69	-3.77	-3.76	-3.73	-3.68
25	-3.13	-3.45	-3.60	-3.71	-3.77	-3.75	-3.72	-3.65
30	-3.21	-3.49	-3.63	-3.73	-3.77	-3.73	-3.66	-3.60
40	-3.33	-3.54	-3.66	-3.73	-3.68	-3.51	-3.36	-3.32
50	-3.37	-3.56	-3.66	-3.68	-3.53	-3.29	-3.25	-3.25
60	-3.36	-3.56	-3.62	-3.63	-3.34	-3.20	-3.20	-3.16
90	-3.37	-3.49	-3.52	-3.27	-3.14	-3.02	-3.00	-3.00
120	-3.06	-3.30	-3.32	-3.10	-2.96	-2.96	-2.87	-2.88

Table D.2: Upper limits of 99%-intervals of pointing deviations.

F-Number	1.8	2.8	4	5.6	8	11	16	22
Exposure [s]								
1	-2.01	-2.04	-2.20	-2.24	-2.37	-2.53	-2.57	-2.08
2	-2.03	-2.19	-2.40	-2.59	-2.75	-2.82	-2.66	-2.53
5	-2.22	-2.49	-2.72	-2.94	-3.08	-3.08	-3.01	-2.75
10	-2.42	-2.72	-2.93	-2.92	-2.82	-2.89	-2.88	-2.75
15	-2.76	-2.83	-2.68	-2.49	-2.47	-2.48	-2.31	-2.22
20	-2.58	-2.80	-3.00	-3.06	-2.92	-2.78	-2.56	-2.59
25	-2.68	-2.82	-2.96	-2.75	-2.61	-2.42	-2.63	-2.54
30	-2.72	-2.84	-2.90	-2.55	-2.52	-2.49	-2.51	-2.46
40	-2.78	-2.79	-2.46	-2.35	-2.17	-2.25	-2.25	-2.16
50	-2.55	-2.61	-2.39	-2.19	-2.15	-2.30	-2.09	-2.18
60	-2.73	-2.12	-2.23	-2.18	-2.10	-2.17	-2.12	-2.03
90	-2.53	-2.21	-2.23	-2.23	-2.13	-2.09	-2.08	-2.06
120	-2.37	-2.11	-2.05	-2.05	-2.03	-2.06	-2.02	-2.03

E Global Rotation Errors in Calibrated Images

Table E.1: Medians of global rotation errors.

F-Number	1.8	2.8	4	5.6	8	11	16	22
Exposure [s]								
1	-2.13	-2.37	-2.54	-2.79	-2.91	-3.04	-3.05	-2.83
2	-2.34	-2.56	-2.75	-2.93	-3.21	-3.23	-3.20	-3.10
5	-2.58	-2.81	-3.08	-3.31	-3.43	-3.49	-3.46	-3.36
10	-2.79	-3.08	-3.31	-3.50	-3.65	-3.66	-3.62	-3.51
15	-2.89	-3.23	-3.43	-3.60	-3.70	-3.67	-3.66	-3.58
20	-3.00	-3.27	-3.48	-3.62	-3.66	-3.71	-3.67	-3.59
25	-3.07	-3.35	-3.52	-3.63	-3.71	-3.72	-3.69	-3.62
30	-3.17	-3.39	-3.56	-3.62	-3.69	-3.72	-3.61	-3.62
40	-3.18	-3.42	-3.54	-3.63	-3.67	-3.67	-3.61	-3.50
50	-3.18	-3.43	-3.60	-3.60	-3.69	-3.61	-3.52	-3.44
60	-3.28	-3.43	-3.58	-3.62	-3.61	-3.52	-3.38	-3.32
90	-3.25	-3.37	-3.46	-3.50	-3.38	-3.24	-3.11	-3.02
120	-2.92	-3.16	-3.26	-3.19	-3.07	-2.80	-2.78	-2.71

Table E.2: Upper limits of 99%-intervals of global rotation errors.

F-Number	1.8	2.8	4	5.6	8	11	16	22
Exposure [s]								
1	-1.56	-1.76	-1.78	-2.00	-1.23	-2.31	-0.71	-1.14
2	-1.67	-1.89	-2.04	-2.27	-2.46	-2.54	-2.37	-2.11
5	-1.86	-2.19	-2.35	-2.66	-2.74	-2.82	-2.57	-2.62
10	-2.13	-2.38	-2.62	-2.70	-2.50	-2.88	-2.56	-2.75
15	-2.24	-2.53	-2.73	-2.73	-2.59	-2.65	-2.31	-2.40
20	-2.33	-2.57	-2.66	-2.15	-2.42	-2.21	-2.57	-2.04
25	-2.39	-2.65	-2.50	-2.53	-2.30	-2.50	-1.91	-2.12
30	-2.42	-2.58	-2.47	-2.54	-2.13	-2.23	-1.75	-1.48
40	-2.53	-1.31	-1.76	-1.51	-1.60	-0.99	-1.72	-1.56
50	-2.57	-1.84	-0.73	-1.85	-1.65	-0.89	-1.50	-1.44
60	-2.14	-1.44	-0.89	-1.03	-0.54	-1.26	-0.82	-1.54
90	-1.44	-1.37	-0.25	-0.84	-0.67	-0.89	-0.95	-0.86
120	-2.04	-1.39	-1.16	-0.47	-0.48	-0.75	-1.14	-1.45

Bibliography

Actis, M., Agnetta, G., Aharonian, F., et al. 2011, Experimental Astronomy, 32, 193

Aharonian, F., Akhperjanian, A. G., Bazer-Bachi, A. R., et al. 2006, Science, 314, 1424

Behera, B., Bähr, J., Grünewald, S., & et al. 2012, Proceedings of SPIE - The International Society for Optical Engineering (Proceedings of SPIE)

Blackett, P. M. S. 1948, in The Emission Spectra of the Night Sky and Aurorae, 34

Carr, J. 2013, Environmental Requirements for CTA, `https://www.cta-observatory.org/`

Castro, D., Slane, P., Patnaude, D. J., & Ellison, D. C. 2011, ApJ, 734, 85

Cherenkov, P. A. 1937, Physical Review, 52, 378

finanzen.net. 2015a, Aluminiumpreis, `http://www.finanzen.net/rohstoffe/aluminiumpreis`, accessed October 12, 2015

finanzen.net. 2015b, Kupferpreis, `http://www.finanzen.net/rohstoffe/kupferpreis`, accessed October 12, 2015

Gaisser, T. K. 1991, Cosmic Rays and Particle Physics (Cambridge University Press)

Galbraith, W. & Jelley, J. V. 1953, Nature, 171, 349

Gillessen, S. 2004, Dissertation, Sub-Bogenminuten-genaue Positionen von TeV-Quellen mit H.E.S.S.

Hamamatsu Photonics K.K. accessed October 11, 2015

Herpich, J. 2010, B. sc. thesis Testing a Single-CCD-Concept for the H.E.S.S. II Pointing

Hofmann, P. 2015, B. sc. thesis Entwicklung eines SingleCCD-Gehäuse-Prototypen im Hinblick auf thermische Eigenschaften

IEEE Computer Society. 2015, IEEE Standard for Ethernet 802.3-2012, `http://standards.ieee.org/getieee802/download/802.3-2012_section1.pdf`, accessed August 18, 2015

Karttunen, H., Kröger, P., Oja, H., Poutanen, M., & Donner, K. J. 2001, Fundamental Astronomy (Springer)

Keicher, B. 2005, AstroPhoto Insight

Lang, D., Hogg, D. W., Mierle, K., Blanton, M., & Roweis, S. 2010, AJ, 139, 1782

Lang et al. 2015, Astrometry.net code README – Astrometry.net 0.40 documentation, `http://astrometry.net/doc/readme.html`, accessed September 6, 2015

Lennarz, D. 2012, Dissertation, Transient Very-High-Energy Gamma-Ray Emission from Gamma-Ray Bursts and Supernovae with H.E.S.S.

Longair, M. S. 1994, High Energy Astrophysics: Volume 2, Stars, the Galaxy and the Interstellar Medium (Cambridge University Press)

Lorenz, E. & Wagner, R. 2012, European Physical Journal H, 37, 459

Mirzoyan, R., Kankanian, R., Krennrich, F., et al. 1994, Nuclear Instruments and Methods in Physics Research A, 351, 513

Moulin, E., Diaz, C., Durand, D., et al. 2015, ArXiv e-prints

Rees, M. J. & Gunn, J. E. 1974, MNRAS, 167, 1

Sedov, L. I. 1959, Similarity and Dimensional Methods in Mechanics (Academic Press)

Specovius, A. 2014, B. sc. thesis Charakterisierung einer astronomischen CCD-Kamera im Rahmen des CTA-Projekts

Taylor, G. 1950, Royal Society of London Proceedings Series A, 201, 159

The Engineering ToolBox. 2015, Metals and Alloys – Densities, `http://www.engineeringtoolbox.com/metal-alloys-densities-d_50.html`, accessed October 12, 2015

USB Implementers Forum. 2015, USB.org – USB FAQ, `http://www.usb.org/developers/usbfaq#cab1`, accessed August 18, 2015

van Eldik, C., Berge, D., Förster, M., & Gaug, M. April 2015, Guidelines for CTA Pointing Calibration

Völk, H. J. & Bernlöhr, K. 2009, Experimental Astronomy, 25, 173

Danksagung

An dieser Stelle möchte ich mich bei Allen bedanken, die mich bei der Erstellung dieser Arbeit unterstützt haben. Vielen Dank an

- Prof. Dr. Christopher van Eldik für die Vergabe des Themas, die zahlreichen Diskussionen und die stets gute Betreuung meiner Masterarbeit.
- Prof. Dr. Gisela Anton für die Übernahme des Koreferats.
- die gesamte CTA/H.E.S.S. Gruppe für das tolle Arbeitklima und die allgegenwärtige Hilfsbereitschft.
- Susanne Raab und Johannes Veh für ihre Zeit beim Korrekturlesen.
- Markus Schindewolf für seine Hilfe in Bamberg, ohne die die Messungen in der Sternwarte nicht möglich gewesen wären.
- Dr. Friedrich Stinzing für die vielen Diskussionen rund um die Hardware-Entwicklung.
- Dipl.-Ing. Klaus Kärcher für die Ausarbeitung der Konstruktionspläne sowie die technische Beratung.
- Philipp Hofmann für die angenehme und konstruktive Zusammenarbeit.
- meine Eltern für die Unterstützung während meines gesamten Studiums.

Erklärung

Hiermit bestätige ich, dass ich die Arbeit selbst verfasst habe und nur die angegebenen Quellen und Hilfsmittel verwendet habe.

Fürth, den 30.10.2015 Domenico Tiziani